Photodegradation of Two Flame Retardants, Including a Phosphate Group, Namely Tris–(2,3-Dichloropropyl) Phosphate (TDCPP) and Tris–(1,3-Dichloro-iso-propyl) Phosphate (TDCIPP) via $NiFe_2O_4$-Based Magnetic Covalent Organic Framework Nanocomposite ($NiFe_2O_4$ - MCOF NC)

DELİA TERESA SPONZA, RUKİYE ÖZTEKİN*
Department of Environmental Engineering
Dokuz Eylül University
Tınaztepe Campus, 35160 Buca/Izmir,
TURKEY

**Corresponding Author*

Abstract: - Metal–organic frameworks exhibited high-performance since can be easily produced in organic substances/metal deposits with enlarged surface area. These properties provide the doping of metal nanocomposites into the porous structure to improve the photocatalytic performance. Therefore, in this study, in order to photodegrade the phosphorous two flame retardants namely tris–(2,3-dichloropropyl)phosphate (TDCPP) and tris–(1,3-dichloro-iso-propyl)phosphate (TDCIPP); NiFe2O4-based magnetic covalent organic framework nanocomposite (MCOF NC) was generated under laboratory conditions. SEM images showed that the NiFe2O4-MCOF nanospheres exhibited fascinating angular and crumpled surfaces with holes, cavities and hollow spaces in the nanocomposite. Both of the NiFe2O4 and NiFe2O4-MCOF NC were composed of C, N, O, Fe, and Ni elements. XPS spectrum of Ni 2p orbital contained two major peaks with binding energy values araund 873.4 eV and 15855.5 eV. A significant weight loss in the nanocomposite was not detected (~2.20%) while an optimal exothermic peak for NiFe2O4–MCOF NC occurred during photodegradation. For maximum TDCPP (99%) and TDCIPP (98%) photodegradation efficiencies the optimazed conditions for contact time, temperature, NiFe2O4–MCOF NC concentration, TDCPP and TDCIPP pollutant concentrations and pH should be 5 min, 40oC, 1.0 mg/l, 1500 mg/l and 5.0, respectively. The photodegradation occurred according to pseudo-first-order reaction kinetic with excellent reusability of NiFe2O4–MCOF NC. Pseudo-first-order photodegradation kinetic showed that the maximum photodegradation rate constants for 1500 mg/l TDCPP and TDCIPP was detected as 0.09 min-1 by 1 mg/l NiFe2O4–MCOF NC. Kinetic studies with adsorption showed although adsorption was detected the majority of pollutants were removed with protodegradation since photodegradation kinetic constants was approximately 8 time higher than that adsorption constants. This showed that photodegradation is the main removal of degradation mechanisms in the removal of TDCPP and TDCIPP under UV ligth. The chronic toxicity of TDCPP and TDCIPP converted to the ″not harmful″ range since their degradation intermediates are significantly less toxic. The aforementioned nanocomposite was reused with yields as high as 99% and 97% for TDCPP and TDCIPP photodegradation, respectively, after 15 cycles.

Key-Words: - Brominated flame retandants (BFRs); Density functional theory (DFT); Flame retardants; NiFe2O4 - based magnetic covalent organic framework nanocomposite (NiFe2O4-MCOF NC); Organophosphorus flame retardants (OPFRs); Photodegradation; Phosphorus-based flame retandants (PFRs); Sun light; Tris–(2,3-dichloropropyl) phosphate (TDCPP); Tris–(1,3-dichloro-iso-propyl) phosphate (TDCIPP).

Received: May 19, 2025. Revised: August 12, 2025. Accepted: November 8, 2025. Published: December 31, 2025.

1 Introduction

The use of phosphorus-based flame retardants (PFRs) is increasingly common in plastics, textiles, and furniture productions. 1,2 Tris(1,3-dichloropropyl) phosphate (TDCPP) is a PFR containing halogen. These PFRs have been replaced by brominated flame retardants (BFRs), which are used in agricultural

equipment and packaging materials. TDCPP is one of the most commonly detected PFRs in environmental and food-related settings. Studies in the literature have revealed that this substance is found in irrigation water, soil, and even agricultural products. This has led to increase its absorption by plants and subsequent entry into the food chain. Tris–(1,3-dichloro-iso-propyl) phosphate (TDCIPP) replaces with penta-BDE in flexible polyurethane foam and is the most prevalent PFR detected in baby products containing flexible polyurethane foam. TDCIPP is a chlorinated analog of tris(2,3-dibromopropyl) phosphate (Tris) which is one of the most detected organophosphorus flame retardants (OPFRs) in the environment, [1], [2].

The United States Environmental Protection Agency (USEPA) estimated and reported that in 2006 the annual production of TDCPP and triphenyl phosphate (TPP) in the United States was between 10 and 50 million pounds. TDCIPP is a persistent organic pollutant and can leach from agricultural plastics and foams used in greenhouses, storage facilities, and irrigation systems, [3].

Owing to adverse biological effects, TDCIPP was subject to a European Union risk assessment process under an Existing Substance Regulation (EEC 793/93) (Regulation 1993), [4]. Recently, it has been determined that TDCIPP causes phenotypic changes and thyroid hormone imbalance in zebrafish larvae, which in turn leads to behavioral abnormalities during zebrafish embryonic development. In addition, TDCIPP has been detected in aquatic biota and humans at levels as high as 6 ppm, [5], [6].

Exposure to TDCPP does not significantly affect the cell viability until at concentration > 68 μg/ml. HCECs show a 16% cell viability loss after exposing to 136 μg/ml TDCPP, [4], [5]. However, TDCPP causes a sharp decrease in viable cell count (87%) after exposure to ≥ 272 μg/ml TDCPP. Based on cell viability, the LC_{50} value for TDCPP is 202 μg/ml using a nonlinear regression. Anti-apoptotic Bcl-2 protein expression increased 1.4-folds after exposing to 2 μg/ml TDCPP, However, significantly decreased at 200 μg/ml compared to the control samples. The caspase-3 activity increased to 2.1 μM, while cell viability and toxicity are affected at higher concentrations (IC_{50} of 171 μM and 168 μM, respectively), [7], [8]. Graphene oxide (GO) has been reported to significantly reduce the mortality and disability rates in zebrafish caused by TDCIPP, by 82% and 48%, respectively, [9].

In a study the photodegradation of TDCPP was performed by using 50 mg/l titanium dioxide (TiO_2) nanoparticle concentration under UV irradiation, by taken into consideration the effects of electrolytes, such as NaCl and NaBr, pH, and temperature, [10]. TiO_2 NPs degraded the TDCPP within 60 min, achieving nearly complete mineralization and release of chloride ions (Cl^-). The decomposition rate decreased inversely as the initial TDCPP concentrations was increased, while it increased proportionally as the TiO_2 dosages was increased. Acidic conditions enhanced the photodegradation, the presence of electrolytes caused nanoparticle aggregation, increasing particle size and thus reduce the photocatalytic efficiency. Chloride (Cl^-) and bromide ions (Br^-) acted as radical scavengers, inhibiting the formation of reactive hydroxyl radicals ($OH^\bullet$). Remarkably, 89% of the total organic carbon (TOC) was removed from the TDCPP after 60 minutes of UV irradiation. This indicates the mineralization of TDCPP into carbon dioxide and water. The degradation intermediates were analyzed using ultrahigh-performance liquid chromatography (UHPLC), and two byproducts were identified after 10 min of treatment. Acute and chronic toxicity analyses revealed that TDCPP's intermediates were nontoxic. Density functional theory (DFT) calculations provide information about electronic structures and decay pathways.

Tris(1-chloro-2-propyl) phosphate (TCIPP) is persistent while TCPP–OH shows the highest improvement in biodegradation and photodegradation (55.48% and 46.37%, respectively), [11]. In biological degradation pathway and photodegradation pathway simulations, it was found that the energy barrier for breaking the phosphate bond in TCPP–OH decreased by 15.73% and 52.52%, respectively, compared to TCPP after modification. The biodegradability and photodegradation efficiency of TCPP–OH was measured to be approximately 75.52% and 77.88%, respectively.

In order to remove the TDCPP in aquatic environments effective treatment, techniques should be developed. In a study some removal mechanisms and toxicity lowering processes were applied for TDCPP degradation through UV-driven hydrogen peroxide process (UV/H_2O_2). The results of this study revealed that the decomposition efficiency of TDCPP with 0.5 mM H_2O_2 reached 88%, which corresponds to a reaction rate constant (k) of 0.04919 min^{-1}, [12]. The widespread presence and ecotoxic properties of TDCPP in aquatic environments necessitate the development of effective and relevant treatment techniques. In a study the results showed that the degradation efficiency of TDCPP reached 95% with 0.5 mM H_2O_2, corresponding to a reaction rate constant (k) of 0.04919 min^{-1}, [13]. Furthermore, three typical chlorinated OPEs (Cl-OPEs) were simultaneously degraded by the UV/H_2O_2 process, with different degradation efficiencies, according to

the following order: TCEP < TDCPP < TCPP. The degradation efficiency was restricted under alkaline condition and in the presence of humic acid (HA), nitrate (NO_3^-), chloride (Cl^-), sulfate (SO_4^{2-}), and dihydrogen phosphate ($H_2PO_4^-$). In the aforementioned study, a total of 12 intermediates formed via different pathways, including bond breaking, hydroxylation, and oxidation reactions, were identified for TDCPP flame retardant. Therefore, it has been determined that longer oxidation times are needed in the UV/H_2O_2 treatment to reduce the toxicity of TDCPP.

Another study investigated the basic reaction mechanisms of typical OPFRs–Tris-(1-chloro-2-propyl) phosphate (TCPP) – under UV/H_2O_2 conditions,[14]. Particular attention was paid to the multi-element (C, H, and O) isotope fractionation during UV/H_2O_2 decomposition, [14]. Results showed that TCPP was rapidly degraded in UV/H_2O_2 system with $OH^\bullet$ radical as the main reactive oxygen species (ROS), leading to a significant oxygen isotope fractionation ($\Delta\delta 18O = -2.98‰$, $\varepsilon O = +2.6 \pm 0.50‰$). Furthermore, phosphorus-oxygen (P-O) bond cleavage was found to be the rate-limiting step through the DFT calculations. No observable hydrogen isotope fractionation and remarkable carbon isotope fractionation ($\Delta\delta 13C = 1.50‰$, $\varepsilon C = -1.9 \pm 0.40‰$) indicated that carbon-chlorine (C-Cl) bond rather than carbon-hydrogen (C-H) bond cleavage was a rate-limiting step. Multi-element CSIA revealed that the UV/H_2O_2 degradation of TCPP initiated by the breaking of P-O and C-Cl bonds. In a study, by combining multi-element CSIA with DFT process is very important mechanisms to determine fate of TCPP in various environments, [14].

In these studies, during the degradation of TDCPP and TDCIPP low removal yields were detected like 69% and 86%, respectively, using UV/H_2O_2. Fe_3O_4 nanoparticles are widely used as magnetic adsorbent materials due to their ease of preparation, controllable size, and superparamagnetic properties. However, these iron oxide magnetic nanoparticles are prone to clumping and to the oxidation in acidic environments. This can lead to a loss of dispersibility and magnetism of the Fe_3O_4 nanoparticles. This negatively impacts their practical applications, [14]. $NiFe_2O_4$, a spinel ferrite, is emerging as a promising alternative due to its moderate saturation magnetization, cost-effectiveness, prevention of aggregation, easy recovery, high mechanical hardness, and stability, [15]. Coating $NiFe_2O_4$ with porous materials such as carbon-based nanomaterials, metal-organic frameworks, and covalent organic frameworks (COFs) the adsorption capabilities can be further enhanced, [16]. COFs, were typical representatives of new porous materials, possess significant advantages like structural order and crystallization, high specific surface area, adjustable pore size, good modifiability, thermal stability, and chemical stability, [17]. They have great potential in the development of structural characteristics and properties, and has become a research hotspot in the field of adsorption and analysis in recent years. In particular, functionalizing COFs and enhancing their hydrophilicity can expand their utility in magnetic separation, enhancing adsorption affinity and retardants specificity for target analytes. Liao et al. prepared a magnetic COFs named $NiFe_2O_4$@TAPB-TPA and used as an MSPE adsorbent for extraction of tetracycline antibiotics, [18]. The limits of detection (LODs) were 0.09–0.26 µg/l, with recovery rates of 91.60–102.70%. Xiang et al. prepared a hydrophobic molecularly imprinted magnetic material (MI-MCOF) with excellent affinity and removal for bisphenol A, [19]. The MSPE method based on MI-MCOF NCs had good application effects in environmental water like beverages and human urine samples at LOD values of 0.020 µg/l at recovery rates of 83.50–110%. Since limited studies was detected on magnetic COFs with $NiFe_2O_4$, the synthesis methods are relatively complex, time-consuming, and highly polluting. The advantages of $NiFe_2O_4$ based COFs have not been yet fully exploited because they have primarily been utilized for analyzing pollutants in liquid samples with simple substrates, [20]. There is a great challenge in reducing of complex animal-derived food substrates using $NiFe_2O_4$ – MCOFs. Therefore, further advanced studied should be performed.

Therefore, this study aimed to develop a selective, sensitive, and effective photodegradation method based on magnetic $NiFe_2O_4$-COF synthesized through a green approach for simultaneous photo-removal of TDCPP and TDCIPP. The main points of this work include: (1) Using a green mechanical grinding method to fabricate $NiFe_2O_4$ based magnetic functional chemical organic framework nanocomposite, (2) Determining the physicochemical properties of the $NiFe_2O_4$- MCOF NC, (3) Investigating the effects of some operational conditions on photo-removals of TDCPP and TDCIPP, (4) Finding of the reusability of the $NiFe_2O_4$-MCOF NC.

2 Materials and Methods

2.1 Synthesis of $NiFe_2O_4$ Nano-catalyst (NC)

The synthesis of $NiFe_2O_4$ nano-catalyst has been described elsewhere, [21], [22]. Our method is

presented with slight modification. The $NiFe_2O_4$ nano-catalyst was synthesized via ultrasonic-assisted co-precipitation method followed by calcination. First, 5 mmol of $Fe(NO_3)_3.9H_2O$ was dissolved in 10 ml distilled water. In the following, 5 mmol of $NiCl_2.7H_2O$ was dissolved in 10 ml of distilled water. Then, two solutions were mixed in a 50 ml beaker. After that, octanoic acid (2 ml, as a surfactant) was slowly poured into the solution. In the next step, NaOH solution (2 M) was dropwise added to the aforementioned mixture with regularly stirring. The pH of the solution was increased to 8.0–9.0. The solution was ultrasonically treated after the entire sedimentation. The optimum time of sonication for crystalline phase generation of nanoparticles was acquired at 60 min/30ºC (250 W, 40 kHz) in this process. Finally, the obtained pink product was gathered with a centrifuge (3000 rpm, 15 min) and rinsed several times by ethanol and distilled water in sequence, and then calcined at 600ºC for 4 h to eliminate any organic residue.

2.2 Preparation of $NiFe_2O_4$ – MCOF NC

In the preparation of $NiFe_2O_4$; $FeCl_3.6H_2O$ (0.84 g), $CO(NH_2)_2$ (0.96 g), and $NiCl_2.6H_2O$ (0.50 g) was dissolved in a Teflon-lined autoclave with 1000 ml deionized water, followed by a vigorous stirring for 60 min. The obtained solution was heated to 180°C for 10 h, which was homogeneous and yellow. After cooling to room temperature, the product was collected by a magnet and washed two times with ethanol and ultrapure water, respectively. Finally, the magnetic $NiFe_2O_4$ was dried in a vacuum oven at 50°C for 10 h.

2.3 Experimental Procedures

Experiments were conducted in a photochemical reactor equipped with four 10 W UV lamps at an irradiation wavelength of 254 nm. The batch experiments were conducted in 15 ml transparent glass test tubes. The TDCPP and TDCIPP concentrations were increased from 500 mg/l up to 3000 mg/l while the photodegradation time elevated from 5 min up to 15 min. $NiFe_2O_4$–MCOF NC concentrations varied between 0.1 and 2.0 mg/l. The pH and temperature were increased from 4.0 up to 8.0 and from 20ºC up to 70ºC, respectively. 8.0 ml of increasing TDCPP and TDCIPP and 2.0 ml of increasing $NiFe_2O_4$–MCOF NC were put in to photochemical reactor at a total volume of 10 ml. The photodegradation experiments were performed at increasing temperatures. Prior to irradiation, the suspension was stirred in the dark for 10 min to achieve an adsorption−desorption equilibrium between TDCPP, TDCIPP and $NiFe_2O_4$–MCOF NC.

2.4 Analytic Methods

At the selected time intervals, 1 ml of the sample was removed, mixed with 3 ml of hexane, extracted using a vortex orbital mixer for 30 min, followed by centrifugation, and analysed using a gas chromatograph (GC, Agilent 6890) equipped with an electron capture detector (ECD). After TDCPP and TDCIPP extractions, the hexane extract phase of the TDCPP and TDCIPP were placed into autosampler vials and analysed by GC-ECD. The column was DB-5 (30 m × 0.32 mm) with a 0.25 mm film. The carrier gas was ultrahigh-purity N_2 (99.999%), with a flow rate of 7 ml/min. The injector temperature was 280°C, and the oven temperature was 100°C, ramped at 40°C/min to 280°C. The detector temperature was 280°C. The retention time of TDCPP and TDCIPP were in the range of 3.2−3.3 min and 2.8-3.00 min, respectively.

The degradation by-products of TDCPP and TDCPP generated during the photocatalytic process were analysed using the ultrahigh-performance liquid chromatography (UHPLC) system (Waters Corporation, Milford, Massachusetts) coupled with an Orbi trap Elite Hybrid Mass Spectrometer and Orbitrap Fusion Lumos Tribrid Mass Spectrometer (Thermo Fisher Scientific, Bremen, Germany). Aliquots from each reaction time were collected, combined into a single solution, and then filtered using a 0.22 μm PVDF membrane filter to remove the catalyst particles prior to analysis. The identification of degradation intermediates was subsequently performed using an UHPLC system.

The Cl^- in the solution was measured by a Thermo Elemental VG PQ ExCell (Thermo Electron) ICP-MS. The samples were pre-rinsed 3 times with 10% HNO_3 (Trace Metal Grade, Fisher Scientific) followed by washing 3 times with ultrapure water. ICP-MS acquisition parameters are instrument detector: simultaneous, dynamic range for chloride: 100–20,000 μg/l, acquisition mode: continuous, peak jumping, No. sweeps: 100, dwell time: 30 ms, channels per mass: 1, acquisition duration: 3.00 s, channel spacing: 0.02 amu, main scan region: ^{35}Cl (34.96 amu), respectively.

The detection method of ion chromatography has high sensitivity and selectivity, but it requires high water quality and is only suitable for testing clean water samples. An ultraviolet detector and a conductivity detector were combined to effectively improve the sensitivity of Cl^- detection. The concentration of Cl^- had a good linear relationship with its peak area. The lower limits for detection and quantification were 9.87×10^{-5} mmol/l and 3.27×10^{-4} mmol/l, respectively, with ion chromatography (IC, Model 861 Advanced Compact IC, Switzerland). After photodegradation, 3 ml TDCPP and TDCIPP

containing treated samples were added to a 15 ml centrifuge tube, placed in an auto sampler, and analysed by IC.

2.5 Separation of $NiFe_2O_4$–MCOF NC from the Treated Samples

All extraction experiments were conducted in 50 ml centrifuge glass tubes. 6 mg of $NiFe_2O_4$–MCOF NC was dispersed into 15 ml wastewater samples. The mixture solution was incubated for 30 min by a slow-moving platform shaker at room temperature. Then, the $NiFe_2O_4$–MCOF NC was collected by applying a magnet to the outer wall of the vial and the supernatant was discarded. Afterwards, the analytes were desorbed from the $NiFe_2O_4$–MCOF NC with 2.5 ml of methanol under static for 10 min, and the eluate was collected by magnetic separation. The collected eluate was dried with a gentle stream of nitrogen (N_2) at room temperature. Finally, the analytes (BFRs) were redissolved in 0.6 ml of methanol.

2.6 Toxicity Analyses of TDCPP and TDCIPP

Toxicity Analyses of TDCPP and TDCIPP using the Ecological Structure Activity Relationships (ECOSAR) predictive program, the structural data of TDCPP and its degradation products were analysed to assess the toxicity levels. This assessment involved the comparison of TDCPP's and TDCIPP's acute and chronic toxicities against established toxic chemicals affecting trophic levels namely daphnid, fish and green algae, [23], [24], [25], [26], [27]. An EC_{50} indicates the concentration needed to cause 50% mortality in green algae after 96 h, while LC_{50} denotes the concentration that results in 50% mortality in daphnids and fish after 48 and 96 h, respectively. The ChV reflect long-term cumulative effects of these chemicals in living organisms. Toxicity was categorized into four levels: very toxic, toxic, harmful, and not harmful, as summarized in Table 1.

* Table 1 can be found in the Appendix section.

2.7 Kinetic Studies

2.7 1 Adsorption

Solute adsorption by a solid in aqueous media typically takes place UV with complicated kinetics. The rate of photo-adsorption under is strongly impacted by a number of parameters relevant to the state of the solid and the physicochemical conditions under that the adsorption happens, [28].

Moreover, photocatalysis is a time-dependent operation and it is essential to measure the photocatalysis rate for designing and assessing the catalyst in eliminating the contaminants from solutions, [29]. The photo adsorption processes of TDCPP and TDCIPP to $NiFe_2O_4$–MCOF NC were investigated by three kinetic models, namely intra-particle diffusion, pseudo-second-order, and pseudo-first-order.

The pseudo-first-order kinetic model can be described by the formula given below, [30], [31], [32], (Eq. 1):

$$Log(q_e - q_t) = logq_e - (k_1/2.303)t (1)$$

Where, q_e and k_1 refer the capacity of removal at equilibrium (mg/g) and rate constants of the pseudo-first order (min^{-1}), respectively. q_t and t are the removal capacity at time t (mg/g) and time of adsorption (min), respectively. The values of k_1 and q_e are acquired from slope and intercept.

Based on pseudo-second-order kinetic model, the rate of photo-adsorption relies upon both adsorptive sites of adsorbent and solute molecules and corresponds to the square product of the difference between the available sites on the adsorbent and the number of occupied sites at equilibrium. The formation of the chemical bond between the solute molecule and the adsorptive site is known as the rate-limiting step. The following equation can describe the pseudo-second-order kinetic model, (Eq. 2):

$$t/q_t = 1/k_2q_e^2 + (1/q_e)t (2)$$

Where, k_2 is the adsorption rate constant of pseudo-second-order kinetic.

The model of intra-particle diffusion is employed to comprehend the process of diffusion. This model describes the solute diffusion from the aqueous phase to the outer surface and thereafter into the inner parts of the pores of the adsorbent because several steps are counted during adsorption. The intra-particle diffusion model is explained by the following equation, (Eq. 3):

$$q_t = k_{dif}\sqrt{t + c} (3)$$

Where, c and k_{dif} denote the thickness of the boundary layer and rate constant of the model of intra-particle diffusion, respectively.

2.7.2 Kinetic studies with Photodegradation

The reaction rate constant (k) was calculated based on the entire degradation period using the pseudo-first-order kinetic model:

$$\ln(C_t/C_0) = -kt (4)$$

Here, C_0 and C_t represent the initial and final concentrations, respectively, and t is the irradiation time.

2.8 Density Functional Theory (DFT) Computational Details

Density functional theory (DFT) computations were performed using the hybrid functional B3LYP method, [33], [34]. The 6-311G(d,p) basis sets, [35], were employed in the Gaussian 09 program to perform a thorough geometry optimization without symmetry constraints. The optimized structure was visualized using GaussView 5.0.8, [36]. Additionally, the natural bond orbital analysis was used for population analysis at the B3LYP/6-311G(d,p) level of theory using the Gaussian 09 software package.

All experiments were carried out three times and the results are given as the means of triplicate samplings. The data relevant to the individual pollutant parameters are given as the mean values.

3 Results and Discussions

3.1 Photodegradation Mechanism

The detailed photodegradation mechanism of $NiFe_2O_4$-MCOF NC was schematically illustrated in Figure 1.

* Figure 1 can be found in the Appendix section.

When $NiFe_2O_4$–MCOF NC photocatalyst is irradiated by UV light, photo-electron moves from the valence band (VB) of the nanoparticle to the empty conduction band (CB). This photon has the energy (hυ) equal to or greater than the band gap. Thus, a hole is created in VB (hVB^+) and an electron (eCB^-) in CB generated as shown in Figure 1 The hole formed in the VB, further reacts with H_2O, then produce $OH^\bullet$ free radical, which act as a powerful oxidizing agent and oxidize adsorbed TDCPP and TDCIPP molecules which are in the near vicinity of $NiFe_2O_4$–MCOF NC surface. Meanwhile, the electrons in (eCB^-) CB, react with O_2 and produce $O^{-2\bullet}$ radicals, which increase the speed of the oxidation process. The $O^{-2\bullet}$ radicals also prevent electron-hole recombination and help in maintaining electrical neutrality in $NiFe_2O_4$–MCOF NC. During the degradation reaction, $O^{-2\bullet}$, further reacts with H^+ formed in the reaction. The protonated hydroperoxyl radical ($HO_2^{-\bullet}$), ultimately produces highly reactive $OH^\bullet$ radical. The generated $OH^\bullet$ radicals constantly attack the TDCPP and TDCIPP structure at different sites like N=N groups, 'Cl' atoms, un-saturation points, etc. During the constant attack of $OH^\bullet$ radicals, the TDCPP and TDCIPP get into stable and hazard free products, [37].

3.2 Characterization of $NiFe_2O_4$ and $NiFe_2O_4$–MCOF NC

3.2.1 SEM Results

SEM was adopted to characterize the information of morphology and structure of the fabricated $NiFe_2O_4$ and $NiFe_2O_4$–MCOF NC nanomaterials. The representative SEM micrographs are shown in Figure 2a and 2b. As indicated in the low magnification SEM images (Figure 2a and 2b), it was apparently demonstrated the products were constituted principally by large amounts of submicronic spherical $NiFe_2O_4$ particles with relatively uniform particle size and uniform dispersion. Figure 3b at higher magnifications reveals the further details of surface morphology for $NiFe_2O_4$–MCOF NC. It was evident that the $NiFe_2O_4$ nanospheres exhibited fascinating angular and crumpled surfaces, which were markedly distinct from those of the previously reported $NiFe_2O_4$–MCOF NC structures, [36], [37]. Furthermore, the SEM images showed the presence of holes, cavities and hollow spaces in the $NiFe_2O_4$–MCOF NC and, indicating the hollow mesoporous structures can be achieved by a one-step solvothermal approach.

* Figure 2 can be found in the Appendix section.

3.2.2 TEM Results

TEM analysis results showed that $NiFe_2O_4$ and $NiFe_2O_4$–MCOF NC were relatively uniform with about 20 nm and 30 nm in diameter, respectively, and displayed a polyhedral morphology (Figure 3a and 3b, respectively). Metal organic framework nanocomposite was successfully coated on the core of $NiFe_2O_4$.

* Figure 3 can be found in the Appendix section.

It is obvious that the $NiFe_2O_4$–MCOF NC particles have cubic-like morphology and their mean size is 50–70 nm in size (data not shown).

3.2.3 EDS Results

The EDS analysis was carried out to explore the element composition of $NiFe_2O_4$ and $NiFe_2O_4$-MCOF NC. Both of the $NiFe_2O_4$ and $NiFe_2O_4$–MCOF NC were composed of C, N, O, Fe, and Ni elements (Figure 4a and 4b). The element mass percentage (wt%) of $NiFe_2O_4$ and $NiFe_2O_4$@MCOFs was 6.99, 0.08, 15.99, 57.68, and 24.19 and 49.88, 1.56, 22.44, 22.01, and 10.06, respectively. As the contents of Fe,

C, and O elements of $NiFe_2O_4$–MCOF NC increased, the results proved that the magnetic organic framework nanocomposite increased by a covalent reaction and the successful modification of the $NiFe_2O_4$ surface was occurred, [38].

* Figure 4 can be found in the Appendix section.

3.2.4 XPS Results

To corroborate the successful synthesis of $NiFe_2O_4$ nanospheres and $NiFe_2O_4$–MCOF NC, the XPS characterizations were performed to investigate the surface composition and chemical state analysis. The survey scan XPS spectrum shown in Figure 5a evidently revealed the existence of Fe, Ni, O, C and N elements according to the observed binding energy peaks. In the narrow scan XPS spectrum of Fe 2p orbital (Figure 5b**),** the prominent peaks located at 710.4 eV and 724.1 eV were ascribed to the core levels of Fe $2p_{3/2}$ and Fe $2p_{1/2}$ of divalent Fe signals, respectively, [39], [40]. As illustrated in Figure 5c, the narrow scan XPS spectrum of Ni 2p orbital contained two major peaks with binding energy values at about 873.4 eV and 855.5 eV accompanied by their corresponding shakeup satellite peaks of 879.8 eV and 861.6 eV, which can be referenced to Ni $2p_{1/2}$ and Ni $2p_{3/2}$ of trivalent Ni signals, respectively (Figure 5d). From the aforementioned results, it was further verified that the $NiFe_2O_4$ nanospheres have been successfully fabricated after the solvothermal process.

* Figure 5 can be found in the Appendix section.

3.2.5 FT-IR Results

The synthesized magnetic materials were further characterized by FT-IR to determine the functional groups of $NiFe_2O_4$, $NiFe_2O_4$–MCOF NC. The obvious absorption peaks at 415 and 606 cm^{-1} were assigned to the stretching vibrations of Fe–O and Ni–O (Figure 6). The band of 1688 and 1694 cm^{-1} were attributed to carboxyl (C=O) stretching vibration. The stretching vibration of C–H of aldehyde group was at 2827 cm^{-1}, and N–H band of the free amino group were at 3318 and 3393 cm^{-1} (Figure 6). The peaks at 1167 cm^{-1} were assigned to C–N deformation vibration of amide bond. The peaks at 1596 cm^{-1} were ascribed to C=N stretching vibration. These results imply the generation of MCOF shells via covalent reaction of TDCPP and TDCIPP.

* Figure 6 can be found in the Appendix section.

As aforementioned, the FT-IR spectra of $NiFe_2O_4$–MCOF NC and $NiFe_2O_4$ are displayed in Figure 6. The main bands of octanoic acid (Figure 6) include broadband at 2650–3450 cm^{-1} corresponding to the stretching vibration of the O–H band at 1718 cm^{-1} corresponding to a carbonyl group. Bands at 1381 and 1461 cm^{-1} also respectively refer to the bending vibrations of CH_3 and CH_2 groups. A band at 941 cm^{-1} and two bands at 1220–1330 cm^{-1} can be assigned to out of plane bending of the O–H group and the stretching of C-O, respectively. The Bands around 876 cm^{-1} and 598 cm^{-1} are respectively related to O-M-O bending vibration and (M: metal) M-O stretching vibration of $NiFe_2O_4$ -MCOF NC, [41].

3.2.6 Nitrogen Adsorption-Desorption Isotherm

The nitrogen adsorption-desorption isotherm was carried out to investigate the porosity of $NiFe_2O_4$ $NiFe_2O_4$–MCOF NC (Figure 7). The BET surface area and the pore volumes of the prepared $NiFe_2O_4$–MCOF NCs were 161.20 m^2/g and 0.47 cm^3/g, respectively. The pore size was about 8.50 nm. The $NiFe_2O_4$–MCOF NC displayed the adsorption isotherm, which revealed the presence of mesoporous.

* Figure 7 can be found in the Appendix section.

Fig. 7: signifies a type III isotherm with an H3 hysteresis loop. The emergence of this type of hysteresis is because of slit-like pores with nonuniform size and/or shape

3.2.7 VSM Curves of $NiFe_2O_4$–MCOF NC

The VSM curves of $NiFe_2O_4$–MCOF NC were shown in Figure 8. The saturation magnetization of $NiFe_2O_4$/organic framework nanocomposite (21.21 emu/g) was lower than that of $NiFe_2O_4$ (33.98 emu/g), which was due to the $NiFe_2O_4$–MCOF NC shell obtained through the covalent reaction of TDCPP and TDCIPP and successfully covered the surface of $NiFe_2O_4$. However, as shown in the inset of Figure 8, $NiFe_2O_4$–MCOF NC could be quickly and completely separated from the sample solution by external magnets in a few seconds.

* Figure 8 can be found in the Appendix section.

The magnetic property of the synthesized photocatalyst was measured utilizing a VSM. Figure 8 also presents the hysteresis loop of $NiFe_2O_4$–MCOF NCs with a magnetic field of 15,000 to 15,000 Oe at room temperature. As illustrated in Figure 8, the saturation magnetization (Ms) of $NiFe_2O_4$–MCOF NC was about 31 emu/g, while its coercivity (Hc) was about 100 Oe. The magnetization profile for the prepared $NiFe_2O_4$–MCOF NC showed a tiny hysteresis behaviour and also had a small value of

coercivity field and residue magnetization. This corroborates that the $NiFe_2O_4$–MCOF NC shows super paramagnetic characteristics at room temperature. This is caused by the $NiFe_2O_4$–MCOF NC demonstrating superparamagnetic characteristics when they are smaller than the critical size of the magnetic domain size.

3.2.8 TGA Analysis

The thermal stability of $NiFe_2O_4$–MCOF NC was evaluated by TGA. Figure 9a shows that the weight loss of $NiFe_2O_4$ and $NiFe_2O_4$-MCOF NC were about 4.60% and 5.55% as the temperature was increased from 45 to 800°C, respectively. The very little weight loss of $NiFe_2O_4$ could be attributed to the loss of adsorbed water and the evaporation of the solvents that are incorporated into the $NiFe_2O_4$ frameworks. However, a slightly weight loss (~8.20%) with a low exothermic peak for the $NiFe_2O_4$–MCOF NC has occurred.

* Figure 9 can be found in the Appendix section.

The $NiFe_2O_4$–MCOF NC show very small change in weight within a temperature interval of 100–810°C, that reveals high phase and temperature stability. The percentage of reduced masses of the coated samples are 2. 90% and 3.20%, respectively. The additional 2% reduction in mass of the MCOF NC was detected in coated $NiFe_2O_4$ sample. The minimum weight loss of the coated samples at higher temperatures shows a great thermal stability.

The materials exhibited degradation in three phases versus high temperatures. For $NiFe_2O_4$-MCOF NCs, the primary step below 200°C accounts for moisture loss on the surface of spinel ferrite, [42]. The second decomposition between the temperature of 31–184°C was attributed to chemicals absorbed during ferrite preparation and the breakdown of the $NiFe_2O_4$ complex, [43]. The third degradation step at temperatures of 519–646°C and 642–681°C was due to the loss of the metal-oxygen bond, [43]. Usually, complete thermal decomposition of spinel ferrite nanoparticles occurs at a temperature of less than 700°C, and the results of the current study agree with the previous thermal stability curve of spinel ferrites, [44], [45], [46], [47]. The fourth degradation step occurred above 665°C and TDCPP and TDCIPP photo degradation chemicals were strongly attached to $NiFe_2O_4$ NCs, [43], [48], [49]. Based on the temperature used for carbonization of TDCPP and TDCIPP, the pyrolysis temperature of the synthesized $NiFe_2O_4$–MCOF NC was within the range of 550°C.

3.2.9 DTA Analysis

The thermal analysis was performed in three diff erent phases. The initial weight loss of 2.50% at between 100–250°C corresponds to the reduction of water molecules and -OH ions from the particle surface. In the second phase of temperature range at between 450–580°C, the weight loss of 3.09% occurred due to the decomposition of the TDCPP and TDCIPP. For the further temperature range (320–700°C), the weight loss of 3.24% occurred due to the formation of pure-phase spinel ferrite (Figure 9b).

3.3 Results of Kinetic Studies

3.3.1 Kinetic Studies with Adsorption

The study of adsorption kinetics of TDCPP and TDCIPP on $NiFe_2O_4$–MCOF NC was performed by the using 3 kinetic models namely intra-particle diffusion, pseudo-first-order, and pseudo-second-order (Table 2)

* Table 2 can be found in the Appendix section.

The kinetic model fitted for pseudo-second-order exhibited a greater regression coefficient (R^2 > 0.9983) than that pseudo-first-order kinetic model (R^2 > 0.9765) and intra-particle diffusion kinetic (R^2 = 0.805) during TPCPP degradation. Additionally, the calculated value of q_e (24 mg/g) for the pseudo-second-order model is close to the experimental value (23.72 mg/g), indicating good fitness of the experimental data with this model. This q_e (24 mg/g) is significantly higher than that found in pseudo-first-order kinetic (q_e = 9.1 mg/g) with higher k_2 values (0.115 min^{-1}) than the aforementioned kinetics (k_1= 0.014 min^{-1} and k_{diff} =0.008 min^{-1} for pseudo first order and intraparticle diffusion, respectively) for TPCPP removal.

During TDCIPP adsorption the kinetic model fitted for pseudo-second-order exhibited a greater regression coefficient (R^2 > 0.9919) than that pseudo-first-order kinetic model (R^2 > 0.9840) and intra-particle diffusion kinetic (R^2 = 0.8145).The q_e and k_2 values in pseudo-second-order kinetic were calculated as 22.701 mg/g, 0.113 min^{-1}, respectively which was higher than that pseudo-first-order kinetic model (q_e=9.1 mg/g and k_1=0.012 min^{-1}) and intra-particle diffusion kinetic (k_{diff}=0.019 min^{-1}), respectively.

The pseudo-second-order kinetic model indicated that the adsorption process is through a chemical reaction rather than a physical reaction, [38]. On the other hand, it can be stated that the rate of adsorption of $NiFe_2O_4$–MCOF NC is not restricted by the mass transfer from bulk liquid to the surface of particle's external only. Moreover, the plotted intra-particle

diffusion model for TDCPP and TDCIPP did not pass through the origin, suggesting that intra-particle diffusion is not the only rate-controlling step for the TDCPP and adsorption mechanism on $NiFe_2O_4$–MCOF NC. The adsorption kinetic data results for the intra-particle diffusion, pseudo-second-order, and pseudo-first-order kinetic models for TDCPP and TDCIPP by $NiFe_2O_4$–MCOF NC is provided in Table 2.

3.3.2 Kinetic Studies with Photodegradation

The pseudo-first-order photodegradation kinetic showed that the maximum photodegradation rate constants for 1500 mg/l TDCPP and TDCIPP was detected as 0.09 min^{-1} by 1 mg/l $NiFe_2O_4$–MCOF NC (Table 3). In the evaluation of these values with the adsorption kinetic constants, the photodegradation kinetic constants was approximately 8 time higher than that adsorption constants. This showed that photodegradation is the main removal of degradation mechanisms in the removal of TDCPP and TDCIPP under UV light. The kinetic rate constants decreased when the initial TDCPP and TDCIPP concentrations increased (Table 3). On the other hand, the reaction rate constants increased with an increase in the $NiFe_2O_4$–MCOF NC from 0.1 to 0.5 and to 1.0 mg/l (Table 3). This concentration-dependent compound removal was also shown in several earlier studies under similar conditions, indicating that the rates of photodegradation of contaminants were strongly influenced by the number of active sites, [45], [46], [47], [49]. The kinetic rate constants of TDCPP and TDCIPP decreased owing to increasing competition with $OH^{\bullet}$ radicals when the initial TDCPP and TDCIPP concentrations were high. Increasing the $NiFe_2O_4$–MCOF NC concentration up to 1.0 mg/l resulted in more active sites during pollutant photodegradations

* Table 3 can be found in the Appendix section.

No more kinetic studies were detected about photodegradation of TDCPP and TDCIPP by $NiFe_2O_4$–MCOF NC.

In a study performed by Mishra et al., [50], UV/H_2O_2-based TDCPP degradation and Escherichia coli deaths were investigated. 90% TDCPP and 80% Escherichia coli removals was detected after 170 min photodegradation in the presence of co-substrate namely tris(chloropropyl) phosphate (TCPP) and tris(2-chloroethyl) phosphate (TCEP). The lowest and highest k values were 1.3×10^{-3} and 3.6×10^{-3} min^{-1} at TCPP concentrations of 10 and 0.10 mg/l, respectively. These values were lower tnan the k values detected in our study. Biswas et al., [51], investigated the structural, optical, and magnetic properties of $NiFe_2O_4$ for efficient photocatalytic degradation of organic pollutants namely methylene blue, rhodamine B, and congo Red. 87-80% photodegradation percentage was detected for dyes a rate constant of 0.0019 min^{-1} and followed pseudo-first-order kinetic model. Wang et al., [52], the effects of $NiFe_2O_4$-based magnetic covalent organic framework nanocomposites on the photodegradation of brominated flame retardants. The adsorption isotherm and the kinetic model were more suitable for Langmuir and pseudo-second-order. Low k values was detected (1×10^{-5} and 1×10^{-5} min^{-1}) during 69 min duration. Low removal yields was detected for 1, 3, 5-Tris-(p- formylphenyl) benzene (TFPB) (69%) and benzidine (Bd) (72%). Nurmayansih et al., [53], found that the small band gap energy of $NiFe_2O_4$ increases the photocatalytic activity of material. Then, the result of photodegradation toward 100 mg/l Congo red showed 71% removal efficiency at a contact time of 25 min at pH=5.7 with a photodegradation rate constant of 1×10^{-5} min^{-1}. Ganesh et al., [54], investigated the photodegradation of azo dyes using MoO_3/$NiFe_2O_4$ nanocomposite. With MoO_3/$NiFe_2O_4$ nanocomposite is found a maximum effciency of 74.47% in 30 min for congo red dye whereas $NiFe_2O_4$ removes only 49.40% and MoO_3 52.04% with low k values of 1.2×10^{-5} and 1.6×10^{-1} min^{-1}. The antibacterial activity of the of Escherichia coli and Staphylococcus aureus decreased to 82% and 86%, respectively. Derakhshania and Ali Naghizadehb, [55], investigated the photodegradation of IBP, IBP influence of persulfate on ibuprofen, rhodamine B, UDMH, chlorpyrifos, ampicillin and sulfamethoxazole using $NiFe_2O_4$-based nanocomposite. Low photodegradation yields were detected (65%-72%) with low photodegradation kinetic constants (1×10^{-5} – 1.9×10^{-5} min^{-1}). The adsorption and photocatalitic yields aforementioned were lower than the our studies performed by 1.0 mg/l $NiFe_2O_4$–MCOF NC to remove the TDCPP and TDCIPP pollutants.

3.4 Effects of Operational Conditions on Photodegradation Yields of TDCPP and TDCIPP

3.4.1 Effects of Initial TDCPP and TDCIPP Concentrations

The amounts of organic compounds adsorbed on the catalyst surface may influence the removal efficiency. However, 1500 mg/l TDCPP and TDCIPP concentrations did not change significantly the photodegradation yields at the beginning indicating that TDCPP and TDCIPP would not adsorb onto the

1.0 mg/l $NiFe_2O_4$–MCOF NC surface in 5 min (Table 4).

* Table 4 can be found in the Appendix section.

Therefore, we can conclude that the TDCPP and TDCIPP concentrations decreased since it was adsorbed onto $NiFe_2O_4$–MCOF NC surface and photodegraded during photodegradation. After 5.0 min duration, 1.0 mg/l $NiFe_2O_4$–MCOF NC almost completely degraded TDCPP and TDCIPP under UV light irradiation (Table 4). When the initial TDCPP and TDCIPP concentrations were around 1500 mg/l, almost 99% TDCPP and 98% TDCIPP yields was detected after 5.0 min whereas approximately 90% TDCPP and 88% TDCIPP degradation was observed when the initial pollutant concentration was increased to 2000 mg/l under the same conditions.

3.4.2 Effect of pH

The effects of pH between 4.0 and 8.0 was investigated on the photodegradation of TDCPP and TDCIPP by 1.0 mg/l $NiFe_2O_4$–MCOF NC (Table 5). During the photodegradation process, the maximum TDCPP and TDCIPP yields was detected at pH=6.0. As the solution pH was increased from 4.0 up to 6.0 the photodegradation yields of TDCPP and TDCIPP increased from 45% to 80% and to 99%. Further increase of pH to 8.0 the yields decreased significantly. The TDCPP and TDCIPP are mineralized to form CO_2 and water. When CO_2 dissolved in the suspension, it reacted with water to form HCO_3^- and H^+, leading to a decrease in the solution pH value.

* Table 5 can be found in the Appendix section.

On the other hand, another significant parameter for an adsorbent is the point of zero charge (pH_{pzc}). It helps in understanding the phenomenon of adsorption and describes the condition at which the surface electrical charge density of the adsorbent is equal to zero, [48], [56], [57], [58], [59], [60], [61]. The pH_{pzc} for $NiFe_2O_4$–MCOF NC was determined as 6.0 (data not shown). The adsorbent surface becomes negatively charged at a pH greater than the pH_{pzc} and positively charged at a pH lower than it. In the present study, we have conducted photodegradation studies at pH=6.0; thereby making the surface of the photocatalyst positive. The outcomes demonstrated that the adsorption was greater at optimum pH ranges because the water solubility of TDCPP and TDCIPP reduces at low pH values. At lower pH conditions, the electrostatic attractive forces between the anionic forms of the positively charged $NiFe_2O_4$–MCOF NC led to a boost in the adsorption capacity of NPs. At higher pHs, repulsion forces between anionic forms of TDCPP and TDCIPP and negatively charged $NiFe_2O_4$–MCOF NC led to a reduction in adsorption of pollutants on the surface of the nanocomposite, as previously reported by other literatures, [62], [63], [64], [65], [66], [67], [68], [69]. Besides, the alkaline conditions lead to a decrease in the oxidation potential of radicals of $OH^\bullet$.

If pH was higher than 6.0, the pH_{pzc} of the $NiFe_2O_4$–MCOF NC and the photodegradation rates of TDCPP and TDCIPP became significantly low. Because TDCPP and TDCIPP are maintained in its molecular state without ionization under different pH conditions, the effects of pH variation on photodegradation mainly resulted from the characteristics of $NiFe_2O_4$–MCOF NC. As aforementioned when the solution pH was lower than pH_{pzc}, the surface of the $NiFe_2O_4$–MCOF NC had a positive charge, which was more favourable for electrons to move from the valence bond (VB) to the covalent bond (CB). This is an essential process for the photocatalytic activity, [49]. Therefore, the recombination of charge carriers was suppressed, resulting in more hole carriers in the VB (h_{vb}^+) reacting with OH^- adsorbed on the surface of the of $NiFe_2O_4$–MCOF NC (OH ads) to generate more $OH^\bullet$ radicals.

3.4.3 Effects of Temperature

The effect of temperature on the photodegradation of TDCPP and TDCIPP by $NiFe_2O_4$–MCOF NC was investigated between 20 and 70°C. The photodegradation efficiencies increased with increasing temperature (Table 6). It was reported that the higher the temperature is, the higher reaction rate is not for $NiFe_2O_4$–MCOF NC. When the temperature reaches 55°C, the reaction rate drops significantly. It has been reported that the photocatalytic activity of $NiFe_2O_4$–MCOF NC increased as the reaction temperature increased up to a limit. Then the TDCPP and TDCIPP photodegradation rates decreased to 65% and 63%. The maximum photodegradation efficiencies of TDCPP and TDCIPP was detected at a 40°C temperature (Table 6).

* Table 6 can be found in the Appendix section.

The photodegradation of TDCPP by P25 NPs was investigated at between 20 and 70°C, [47]. The rate constants increased with increasing temperature, which corresponds to general chemical reactions. The k values were used to calculate the activation energy of the photodegradation of TDCPP using the Arrhenius equation (Eq. 5), [47]:

$$lnk = lnA - \frac{E_a}{RT}(5)$$

Where, k is the rate constant of the pseudo-first-order model (1/min), A is the Arrhenius coefficient, E_a is the activation energy (kJ/mol), R is the gas constant (8.314 J/mol·K), and T is the absolute temperature in kelvin (^oK). The activation energy was determined from the slope of the lnk versus 1/T plot. The activation energy of the photodegradation of TDCPP by P25 NPs was 5.58 kJ/mol (R^2=0.992), which was relatively low.

3.4.4 Effect of Contacting Time

The effect of contact time on photodegradation efficiency was examined using 1500 mg/l TDCPP and TDCIPP concentrations and 1.0 mg/l $NiFe_2O_4$–MCOF NC from 5 min to 60 min. Table 7 showed that an increase in the contact time led to a decrease in residual TDCPP and TDCIPP concentrations. The highest removal efficiency was observed at 5 min. There is no previous work on the use of $NiFe_2O_4$–MCOF NC at varying temperatures to can compare the present data. As the contact time increases, the rate of photodegradation first increases and then becomes almost constant. This is due to the aggregation of TDCPP and TDCIPP metabolites with the increase in contact time, which makes it almost impossible to diffuse deeper into the $NiFe_2O_4$–MCOF NC structure at higher energy sites. This aggregation inhibits the influence of contact time as the pores get filled up and start offering resistance to diffusion of aggregated TDCPP and TDCIPP molecules in the surface of $NiFe_2O_4$–MCOF NC. It has been seen that the equilibration time of 5 min is sufficient since maximum photodegradations are attained during this period.

* Table 7 can be found in the Appendix section.

Time of irradiation plays a crucial role in the elimination of pollutants from wastewater. The impact of irradiation time on the percent adsorption of individual by $NiFe_2O_4$–MCOF NC was examined for at increasing pollutant concentrations by increasing the time from 5 min up to 60 min. The removal efficiencies of TDCPP and TDCIPP photodegradation are a function of irradiation time. It was established that the photodegradation efficiency decreased during increasing irradiation time. The maximum photodegradation irradiation time was obtained at 5.0 min. Actually, it can be found that at 5.0 min the molecules of TDCPP and TDCIPP possess a sufficient chance for adsorption on the catalyst surface and photodegraded utilizing UV irradiation.

3.4.5 Effect of $NiFe_2O_4$–MCOF NC Concentration

Table 8. showed the effect of catalyst dosage on photodegradation yields of TDCPP and TDCIPP. The degradation efficiency was highest at 1.0 mg/l NiFe2O4–MCOF NC concentration (Table 8). At higher nanocomposite dosage, the degradation was found to decrease. One of the possible reasons might be the turbidity of the solution, which increased with the amount of catalyst and blocked the photons reaching the medium. This phenomenon may result to a smaller number of active photoactive species and consequently reduction in percentage of degradation. Several studies report the photocatalytic rate to first rise along with catalyst loading and then deflate at high dosage due to unavailable active surface sites for exposure and light scattering effects, [47], [48]

* Table 8 can be found in the Appendix section.

By rising of $NiFe_2O_4$–MCOF NC dosage, the TDCPP and TDCIPP interaction with the catalyst led to increase of the TDCPP and TDCIPP photodegradation yields. As the $NiFe_2O_4$–MCOF NC concentration was increased from 0.1 mg/l to 1.0 mg/l the pollutant yields increased from 45% up to 99%. This can be recognized because of the availability of a large amount of local active sites to adsorb molecules of TDCPP and TDCIPP. Moreover, utilizing greater quantities of the photocatalyst (2.0 mg/l) led to decreasing the quantity of adsorbed TDCPP and TDCIPP resulting in decreasing of the quantity of the photogenerated oxidizing radicals.

3.4.6 Reusability Studies

The photocatalytic reusability of the synthesized photocatalyst was investigated via stability test. The photocatalytic reusability test of the photocatalyst was studied for TDCPP and TDCIPP photodegradation up to 20 cycles (Table 9). The degradation efficiency of TDCPP and TDCIPP were slightly decreased slightly during the 20 consecutive cycles. The slightly decrease in degradation efficiency could be attributed to the slightly loss of the nanocomposite amount,[47]. The small decrease in the numbers of active cites in the $NiFe_2O_4$–MCOF NC lowered the TDCPP and TDCIPP

efficiency during photodegradation ending with slightly low reusability.

* Table 9 can be found in the Appendix section.

3.4.7 TDCPP and TDCIPP Degradation Metabolites

After 5 min photodegradation period, two primary intermediates were identified namely TP313 ($C_6H_{10}Cl_3O_6P$) and TP207 ($C_3H_7Cl_2O_4P$) during TDCPP photodegradation (Table 10). The degradation mechanism appears to proceed through an initial attack by $OH^{\bullet}$ radicals on the $C_3H_5Cl_2-O$ and C−Cl bonds of TDCPP. This leads to oxidation reactions that facilitate the formation of a carboxylic acidic group, resulting in the formation of intermediate TP313, [70], [71]. Subsequently, TP313 undergoes dichlorination, followed by hydroxylation, to yield the second intermediate, TP207. This sequential degradation pathway highlights the critical role of $OH^{\bullet}$ radicals in breaking down TDCPP into progressively simpler intermediates via oxidation, dichlorination, and hydroxylation reactions. The degradation of TDCPP indicated that the final byproducts of this process are CO_2, H_2O, and Cl^-. This finding confirms that TDCPP undergoes complete mineralization during phodegradation, resulting in nontoxic end products. The degradation mechanism of TDCPP can be understood by examining its molecular orbital characteristics and comparing them with those of the observed intermediates, TP313 and TP207.

The main mechanisms involved the TDCIPP ($C_9H_{15}Cl_6O_4P$) photo degradation included bond breaking by hydroxylation and oxidation. Four possible degradation pathways like bond breaking reaction path, hydroxylation reaction path, oxidation reaction path, and bond breaking and oxidation reaction path were proposed for photodegradation of TDCIPP, [72]. Path I consisted of TP317 (diphenyl phosphate, m/z, 318.9218) and TP207 (monophenyl phosphate, m/z, 208.9529) metabolites consisting of bond breakings during photodegradation (Table 10). During TDCIPP photodegradation, the produced intermediates were TP407, TP389 and TP409 and these metabolites are observed in Path IV (Table 10). Moreover, five oxidation and bond-breaking products were formed through Path IV, including TP313 (m/z, 314.9349), TP297 (m/z, 298.9400), TP203 (m/z, 204.9659), TP187 (m/z, 188.9712), and TP170 (m/z, 171.0055). The formation of the bond-breaking products might involve two steps. Firstly, oxygen-1,3-dichloropropyl formed from the phosphoric centre in TDCIPP molecule and was detached due to the attack of OH, following the degradation reaction towards $OH^{\bullet}$ that occurred through the addition of an H_2O molecule with electron transport chains. This led to the formation of TP317 and TP207, [72], [73]. Path II included two hydroxylation products, namely TP409 (m/z, 410.9261) and TP299 (m/z, 300.9555). The C-Cl bonds on the TDCIPP chain ends with TP317 production when OH radical was attached. As a results Cl^- was released and, consequently, TP409 and TP299 were produced. In addition, TP299 might also be generated from TP409 through breaking of the bonds during photo reaction. Path III consisted of three oxidation products, namely TP423 (m/z, 424.9038), TP407 (m/z, 408.9090), and TP389 (m/z, 390.9427), formed through oxidation reactions involving the hydroxylation products. For example, TP409 resulted during formation of aldehyde and, therefore, TP407 was generated. Specifically, tetroxide was generated during TP409 production by bimolecular self-termination reactions, followed by a unimolecular decomposition process to form the aldehyde group. This group was subsequently oxidized into a carboxyl group through the effect of $OH^{\bullet}$, resulting in the formation of TP423, [67]. TP407 might also generate TP389 through the transformation mechanism of TDCIPP via hydroxylation reaction. According to a recent study, based on the Fukui function, the phosphate and halogen groups of the TDCIPP were the potential attack sites by free radicals via UV/H_2O_2 process, [72]. In a recent study, TP170 was formed from TP389 through the bond-breaking reaction of TDCIPP, while TP313 and TP203 were both obtained via detaching of oxygen-1,3-dichloropropyl groups from TP423 intermetabolite, [74].

The main intermediates of TDCPP and TDCIPP was shown in Table 10.

* Table 10 can be found in the Appendix section.

After 5 min of photodegradation, two primary intermediates, identified as TP313 ($C_6H_{10}Cl_3O_6P$) and TP207 ($C_3H_7Cl_2O_4P$), were detected from the photodegradation of TDCPP. The proposed degradation pathways for these intermediates and Discrete Fourier Transform (DFT) Analysis results for TDCPP is illustrated in Figure 10.

* Figure 10 can be found in the Appendix section.

3.4.8 Discrete Fourier Transform (DFT) Analysis for TDCPP

The optimized molecular structure of TDCPP was obtained by DFT calculations. This optimization minimizes the molecule's energy, revealing its most stable conformation. The optimized geometry serves as the foundation for further electronic structure analyses, including natural bond orbital (NBO) analyses, highest occupied molecular orbit (HOMO), and lowest unoccupied molecular orbit (LUMO), helping to identify reactive sites and understand how TDCPP undergoes photocatalytic degradation.

NBO analysis further supports this by indicating a lower electron density or stability in these bonds, making them likely sites for hydrolysis or dechlorination. The breakdown of TDCPP through these pathways highlights the relative weakness of the C-Cl and P=O bonds under oxidative conditions, as observed in other phosphate-based flame retardants, [75], [76]. The HOMO of TDCPP, concentrated around electronegative atoms like the phosphorus−oxygen (P=O) group and chlorine-substituted carbon atoms, indicates sites of high electron density that are more prone to oxidative attacks (Table 11). These regions, particularly the P=O group, may serve as initial targets for hydroxylation, consistent with the first transformation step leading to TP313 via hydroxylation and carboxylation, [77].

* Table 11 can be found in the Appendix section.

The LUMO analysis suggests areas that may be vulnerable to nucleophilic attacks, potentially facilitating bond cleavage or further transformation, especially near the P=O and C−Cl bonds (Table 11). This vulnerability aligns with the stepwise dechlorination observed in TDCPP's degradation pathway, where C−Cl bonds progressively break, leading to the formation of TP207 (Table 10). Although, photogenerated electrons (e^-) in $NiFe_2O_4$–MCOF NC primarily reduce oxygen to form O^{-2} • radicals, DFT analysis indicates that the HOMO of TDCPP is located on electron-rich sites (P=O and chlorinated carbons), which are highly susceptible to attack by electrophilic OH. These OH• radicals, generated from photogenerated holes in $NiFe_2O_4$–MCOF NC, act as the main oxidizing agents for TDCPP. Direct electron transfer to TDCPP by photogenerated electrons is considered minimal. Comparing the intermediates TP313 and TP207 with the DFT findings suggests a coherent mechanism: the electron rich P=O bond initiates hydroxylation, while the less stable C−Cl bonds undergo sequential dechlorination. This degradation pathway illustrates how TDCPP's structural features, identified through molecular orbital analysis, determine its reactivity and susceptibility to environmental breakdown, [78], [79]. These insights not only elucidate the degradation process of TDCPP and TDCIPP but also provide a foundation for predicting similar transformations in related compounds.

3.5 Toxicity Analyses Results of TDCPP and TDCIPP

Toxicity analyses results of TDCPP and TDCIPP and also some intermediates were summarized in Table 12.

* Table 12 can be found in the Appendix section.

The acute LC_{50} of fish and daphnid were calculated as 5.29 and 10.8 mg/l for 1500 mg/l TDCPP, respectively, while LC_{50} values increased to 39,254 and 19,785 mg/l and to 2541 and 1267 mg/l in the presence of metabolites namely TP313 and TP207, respectively. This indicated that during photodegradation and cleaving of $C_3H_5Cl_2$−O bonds via −OH radicals the acute toxicity decreased significantly. For green algae the EC_{50} was measured as 3.96 mg/l for TDCPP, while this value increased to 8912 mg/l and 571 mg/l during photocatalysis since the productions of intermediates namely TP313 and TP207 are low toxic than parent TDCPP, respectively. Both intermediates exhibited lower toxicity than that parent TDCPP, leading to a rapid detoxification during the photo catalytic reaction process. For chronic toxicity, TDCPP shows a significant toxicity with ChV values of 0.44 mg/l for fish, 2.03 mg/l for daphnid, and 1.47 mg/l for green algae, maintaining its classification as ″toxic″. TP313 and TP207 display much lower chronic toxicities. With the production TP313, the LC_{50} values were recorded as 3326 mg/l for fish, 1384 mg/l for daphnids with EC_{50} values of 1784 mg/l for green algae. TP207 has a ChV values of 210 mg/l for fish, 88.5 mg/l for daphnid, and 113 mg/l for green algae, both remaining in the ″not harmful″ range (Table 12).

The acute LC_{50} values for fish and daphnid were found as 5.29 and 10.8 mg/l for 1500 mg/l TDCIPP, respectively, while LC_{50} values increased to 20,962 and 41,312 mg/l as the TDCIPP converted to metabolites namely BDCPP and TDBPP. As shown the acute toxicity decreased significantly for both organisms. For green algae the EC_{50} was measured as 4.02 mg/l for TDCIPP, while this value increased to 9226 mg/l in the presence of BDCPP metabolite while in the production of TDBPP metabolite the EC_{50} value increased to 612 mg/l (Table 12). The chronic toxicity test analyses show that, TDCIPP exhibited a significant initial toxicity with ChV values of 2.75 mg/l for fish, 0.52 mg/l for daphnid, and 1.90 mg/l for green algae, maintaining its classification as ″toxic″. as the photodegradation products were released, the ChV values also increased. during production of BDCPP metabolite the ChV values increased to 1412 mg/l, to 3540 mg/l and to 1846 mg/l for Daphnid, fish and green algae, respectively. During the production of TDBPP metabolite ChV values of Daphnid, fish and green algae increased to 97.3 mg/l, 275 mg/l and to 126 mg/l, respectively. The chronic toxicity converted to the ″not harmful″ range.

These results indicate that TDCPP and TDCIPP are significantly more toxic in both acute and chronic

exposure scenarios compared to their degradation intermediates. Overall, the data indicate that both TP313 and TP207 metabolites are significantly less toxic than TDCPP while BDCPP and TDBPP are the photodegradation metabolites of TDCIPP demonstrating the effectiveness of the degradation process in mitigating the environmental risks associated with this flame retardant. This study demonstrates the effective photocatalytic degradation of TDCPP and TDCIPP using $NiFe_2O_4$–MCOF NC under UV irradiation. The degradation process achieved nearly complete removals of TDCPP and TDCIPP within 5.0 min, accompanied by significant mineralization.

3.6 Production Cost

Compared with conventional composite materials, nanomaterial-based composites are not expensive to produce because of the need for green synthesis techniques, and reuse of nanocomposite. These factors contribute to not elevated overall manufacturing costs for the final nanocomposite products. In addition, the lowest costs associated with synthesizing materials at the nanoscale, designing and testing various nanomaterials before their utilization, and developing optimal compositions to enhance the properties of the resulting nanocomposite further contribute to the economic challenges of manufacturing. Hence, for certain essential applications, the high costs of nanocomposite production may render them economically non-feasible. Minimizing the production costs of nanocomposites can be addressed by implementing efficient and cost-effective manufacturing processes.

In this study, in order to remove the TDCPP and TDCIPP with yields as high as 99% and 98% the cost of 1.0 g $NiFe_2O_4$–MCOF NC was calculated as 0.05 Euro by taken into consideration the reusability of the aforementioned nanocomposite with the same yields after 15 cycles. The cost of the UV light for 5 min was calculated as 0.01 euro.

The recycling processes of the nanocomposite will not only contribute to cost savings but also significantly minimize the environmental impact. In the use of sunligth instead of UV light the cost should be effectively minimized.

3.7 Environmental Impact

Nanocomposites offer a range of promising properties and applications across various industries. However, like any emerging technology, the environmental impact of nano-based nanocomposites warrants careful consideration, as it depends largely on the different types of nanoparticles used in composite development. Handling and disposal of nano-based nanocomposites can release nanoparticles into the environment, which may have adverse effects on ecosystems and human health if they are not properly managed. The small size of nano-based materials can make them very reactive and potentially hazardous to humans and the environment in general. Nanoparticles can penetrate many biological barriers, such as cell membranes, and may harm cells, tissues, and lungs. Some nanomaterials used in nanocomposites have shown potential toxicity under certain circumstances. The behavior of nanoparticles in the environment under different conditions has not been documented. Understanding their behavior will help mitigate any adverse effects they may have on ecosystems and human health. In the nanocomposite development, the addition of nanomaterials such as carbon nanotubes or metal nanoparticles can undermine their eco-friendly properties. Many synthetic nanomaterials do not break down naturally, leading to long-term environmental accumulation and posing risks to ecosystems and biodiversity. In this study, the acute and chronic toxicity tests on $NiFe_2O_4$–MCOF NC showed no toxicity (data not shown).

Therefore, it is essential to carefully manage the production and use of nanomaterials in composite development and other applications by conducting comprehensive life cycle assessments (LCAs) to evaluate the environmental impacts associated with nano-based nanocomposites. This involves evaluating the environmental footprint of these materials from raw material extraction to end-of-life disposal.

Governments and international organizations must develop policies and guidelines to address environmental concerns and minimize potential risks. Finally, the exploration of green-based nanomaterials and green-synthesized metal nanoparticles in nanocomposite development is essential. This exploration, coupled with the adoption of more eco-friendly manufacturing processes, will address these environmental and health concerns without significantly compromising their performance and functionality.

4 Conclusions

A new kind of $NiFe_2O_4$-based MCOF NC was fabricated through facile synthesis approach to remove the TDCPP and TDCIPP. This nanocomposite exhibited higher photodegradation efficiency for BFRs containing phosphate group based on hydrophobic interactions and π-π stacking interaction.

The effective parameters, such as initial concentrations of TDCPP and TDCIPP, dosage catalyst, equilibrium time, temperature, and solution of the pH were optimized. The optimum conditions for

photodegradation of TDCPP and TDCIPP were acquired at pH=6.0, at an irradiation time of 5 min, at a $NiFe_2O_4$–MCOF NC concentration of 1.0 mg/l, at a temperature of 40^oC, and at a BFR concentration of 1500 mg/l, respectively. The kinetic results indicated that pseudo-second-order kinetic equations revealed a better agreement with the adsorption process compared to other examined adsorption models. The main removal mechanisms of TDCPP and TDCIPP was found to be photodegradation with a six time higher pseudo-second-order reaction constant compared to adsorption kinetic constants. The chronic and acute toxicity of TDCPP and TDCIPP organics decreased to not toxic level. The reusability of the $NiFe_2O_4$-MCOF NC over 15 cycles with minimal loss and 99% and 97% TDCPP and TDCIPP efficiencies supports its practical applicability in the wastewater treatment processes. This indicates the suitability of magnetic photocatalyst in treatment of toxic brominated compounds.

These findings provide critical insights into the degradation behaviour of halogenated organophosphorus flame retardants in aquatic environments and support the development of advanced photocatalytic systems for environmental remediation.

Acknowledgement:
Experimental analyzes in this study were performed at the Laboratories of the Canada Research Center, Ottawa, Canada. The authors would like to thank this body for providing financial support.

References:

[1] P. Xiang, R.-Y. Liu, C. Li, P. Gao, X.-Y. Cui, L. Q. Ma, Effects of Organophosphorus Flame Retardant TDCPP on Normal Human Corneal Epithelial Cells: Implications for Human Health, Environmental Pollution, Vol.230, 2017, pp. 22-30.

[2] D. W. Killilea, D. Chow, S. Q. Xiao, C. Li, M. L. Stoller, Flame Retardant Tris(1,3-dichloro-2-propyl)phosphate (TDCPP) Toxicity is Attenuated by N-Acetylcysteine in Human Kidney Cells, Toxicology Reports, Vol.4, 2017, pp. 260-264.

[3] K. Hoffman, L. Gearhart-Serna, M. Lorber, T. F. Webster, H. M. Stapleton, Estimated Tris(1,3-dichloro-2-propyl) Phosphate Exposure Levels for U.S. Infants Suggest Potential Health Risks, Environmental Science & Technology Letters, Vol.4, No.8, 2017, pp. 334–338.

[4] Y. Yang, Y. Pu, C. Liu, L. Gao, X. Duan, S. Liu, D. Chen, L. Zhong, Y. Li, Environmentally Relevant Concentrations of Tris (1,3-dichloro-2-propyl) Phosphate Induce Growth Inhibition and Oxidative Stress in Silver Carp (Hypophthalmichthys molitrix) Larvae, Ecotoxicology and Environmental Safety, Vol.241, 2022, 113798.

[5] D. Desantis, Y. Yang, K. P. Lai, R. S. S. Wu, C. Schunter, Sex-Specific Neurotoxicity and Transgenerational Effects of an Emerging Pollutant, Tris(1,3-dichloro-2-propyl)phosphate (TDCIPP), Science of The Total Environment, Vol.957, 2024, 177520.

[6] Y. H. Ning, Y. Xu, J. Y. Bao, W. P. Wang, A.-J. Wang, β-Cyclodextrin-Functionalized Magnetic Graphene Oxide for the Efficient Enrichment of Bisphenols in Milk and Milk Packaging, Journal of Chromatography A, Vol.1692, 2023, 463854.

[7] X. Ren, Z. Liu, R. Zhang, Y. Shao, X. Duan, B. Sun, X. Zhao, Nanoplastics Aggravated TDCIPP-Induced Transgenerational Developmental Neurotoxicity in Zebrafish Depending on the Involvement of the Dopamine Signalling Pathway, Environmental Toxicology and Pharmacology, Vol.108, 2024, 104436.

[8] T. Cang, W. Gu, Y.-C. Zhu, M. Guo, L. Lv, C. Wu, Y. Jin, Y. Wang, Environmental Concentrations of TCEP and TDCIPP Induce Dysbiosis of Gut Microbiotal and Metabolism in the Honeybee (Apis mellifera L.), Journal of Hazardous Materials, Vol.491, 2025, 138039.

[9] W. Zou, X. Zhang, S. Ouyang, X. Hu, Q. Zhou, Graphene Oxide Nanosheets Mitigate the Developmental Toxicity of TDCIPP in Zebrafish via Activating the Mitochondrial Respiratory Chain and Energy Metabolism, Science of The Total Environment, Vol.727, 2020, 138486.

[10] M. Chang, T. A. Geleta, H.-J. Chen, Y.-h. Shih, Rapid Tris(1,3-dichloropropyl) Phosphate Degradation and Detoxification via TiO2 Nanoparticles under UV Light: Kinetics and Mechanism, Environmental Implications, and Insights into DFT, ACS Agricultural Science & Technology, Vol.5, No.7, 2025, pp. 1400−1412.

[11] J. Yang, Q. Li, Y. Li, Enhanced Biodegradation/Photodegradation of Organophosphorus Fire Retardant Using an Integrated Method of Modified

Pharmacophore Model with Molecular Dynamics and Polarizable Continuum Model, Polymers, Vol.12, No.8, 2020, 1672.

[12] Z. Luo, L. Yuan, J. W. C. Wong, M. Zhu, Y. Yu, K. Wang, H. Yin, S. Tang, J. Niu, Degradation of Tris(1,3-dichloro-2-propyl) Phosphate (TDCPP) by Ultraviolet Activated Hydrogen Peroxide: Mechanisms, Pathways and Toxicity Assessments, Chemical Engineering Journal, Vol.497, 2024, 155690.

[13] J. Xiong, Y. Guo, S. Chen, Z. Wang, G. Li, F. Gelman, M. Wen, Y. Gao, T. An, The Underlying Degradation Mechanisms of Typical Organophosphorus Flame Retardants in Water Based on Identified Intermediates and C, H and O Isotope Fractionation, Journal of Environmental Chemical Engineering, Vol.13, No.3, 2025, 116223.

[14] G. Rana, P. Dhiman, A. Kumar, D.-V. N. Vo, G. Sharma, S. Sharma, M. Naushad, Recent Advances on Nickel Nano-Ferrite: A Review on Processing Techniques, Properties and Diverse Applications, Chemical Engineering Research and Design, Vol.175, 2021, pp. 182-208.

[15] W. K. Li, Y. P. Shi, Recent Advances and Applications of Carbon Nanotubes Based Composites in Magnetic Solid-Phase Extraction, Trends in Analytical Chemistry, Vol.118, 2019, pp. 652-665.

[16] K. X. Hu, L. Chen, S. Gao, W. R. Liu, B. Wei, Q. H. He, Application Progress of Covalent Organic Frameworks (COFs) Materials in the Detection of Food Contaminants, Food Control, Vol.155, 2024, Article: 110072.

[17] W. L. Liao, Y. Xu, D. Y. Li, Y. X. Ye, Y. H. Ning, W. P. Wang, A. J. Wang, Facile Room Temperature Synthesis of a NiFe2O4-Based Magnetic Covalent Organic Framework for the Extraction of Tetracycline Residues in Environmental Water Samples Prior to HPLC, Analytical Methods, Vol.14, 2022, pp. 4938-4946.

[18] J. X. Xiang, P. P. Zhou, H. Mei, X. D. Liu, H. L. Wang, X. D. Wang, Y. Y. Li, Highly Efficient Nanocomposites Based on Molecularly Imprinted Magnetic Covalent Organic Frameworks for Selective Extraction of Bisphenol A from Liquid Matrices, Microchimica Acta, Vol.190, 2023, Article number: 200.

[19] S. Lin, Y.-k. Lv, A. Zhu, M. Su, X. Li, S.-x. Liang, Development of a NiFe2O4 Covalent Organic Framework Based Magnetic Solid-Phase Extraction Approach for Specific Capture of Quinolones in Animal Innards Prior to UHPLC–Q–Orbitrap HRMS Detection, Food Chemistry, Vol.454, 2024, 139796.

[20] J. Regnery, W. Puettmann, Occurrence and Fate of Organophosphorus Flame Retardants and Plasticizers in Urban and Remote Surface Waters in Germany, Water Research, Vol.44, No.14, 2010, pp. 4097−4104.

[21] S. Sendhilnathan, P.I. Rajan, T. Adinaveen, Synthesis and Characterization of NiFe2O4 Nanoparticles for the Enhancement of Direct Sunlight Photocatalytic Degradation of Methyl Orange, Journal of Superconductivity and Novel Magnetism, Vol.31, No.10, 2018, pp. 3315–3322.

[22] A. Shokri, Using NiFe2O4 as a Nano Photocatalyst for Degradation of Polyvinyl Alcohol in Synthetic Wastewater, Environmental Challenges, Vol.5, 2021, 100332.

[23] S.-E. Huang, K.-H. Tan, R. S. Sahu, T. A. Geleta, A. Miri, C.-Y. Lin, Y.-H. Shih, W.-L. Chen, Facile Synthesis and Optimization of Graphitic Carbon Nitride Nanoparticles to Effectively Photodegrade Tetracycline under Visible Light in Water, ACS Agricultural Science & Technology, Vol.5, No.2, 2025, pp. 235−245.

[24] S. Tang, Z. Luo, J. Liao, Z. Liu, L. Xu, J. Niu, Degradation and Detoxification Mechanisms of Organophosphorus Flame Retardant Tris (1, 3-Dichloro-2-Propyl) Phosphate (TDCPP) during Electrochemical Oxidation Process, Chinese Chemical Letters, Vol.34, No.8, 2023, 108090.

[25] Q. Sui, W. Gebhardt, H. F. Schörder, W. Zhao, S. Lu, G. Yu, Identification of New Oxidation Products of Bezafibrate for Better Understanding of its Toxicity Evolution and Oxidation Mechanisms during Ozonation, Environmental Science & Technology, Vol.51, No.4, 2017, pp. 2262−2270.

[26] K. S. Tay, N. Madehi, Ozonation of Ofloxacin in Water: by Products, Degradation Pathway and Ecotoxicity Assessment, Science of the Total Environment, Vol.520, 2015, pp. 23−31.

[27] T. A. Geleta, R. Q. Tee, Y.-H. Shih, W.-L. Chen, Exploring Charge Transfer and Degradation Mechanism of One-Step Synthesized Modified g-C3N4 for Efficient Photocatalytic Bisphenol A Removal under

Visible Light, Colloids and Surfaces A: Physicochemical and Engineering Aspects, Vol.719, 2025, 136990.

[28] M. J. Culzoni, A. V. Schenone, N. E. Llamas, M. Garrido, M. S. Di Nezio, B. S. F. Band, H. C. Goicoechea, Fast Chromatographic Method for the Determination of Dyes in Beverages by Using High Performance Liquid Chromatography—Diode Array Detection Data and Second Order Algorithms, Journal of Chromatography A, Vol.1216, No.42, 2009, pp. 7063–7070.

[29] F. Nekouei, S. Nekouei, Comparative Evaluation of BiOCl–NPls–AC Composite Performance for Methylene Blue Dye Removal from Solution in the Presence/Absence of UV Irradiation: Kinetic and Isotherm Studies, Journal of Alloys and Compounds, Vol.701, 2017, pp. 950–966.

[30] S. P. Hooshyar, H. A. Panahi, E. Moniri, M. Farsadrooh, Tailoring a New Hyperbranched PEGylated Dendrimer Nano-Polymer as a Super-Adsorbent for Magnetic Solid-Phase Extraction and Determination of Letrozole in Biological and Pharmaceutical Samples, Journal of Molecular Liquids, 2021, 116772.

[31] S. H. Khoshravesh, Z. Azizi, H. Javadian, M. Farsadrooh, N. Hashemifard, M. Soltani, M. Taghavi, Synthesis of Resorcinol-Functionalized Multi-Walled Carbon Nanotubes as a Nanoadsorbent for the Solid-Phase Extraction and Determination of Diclofenac in Human Plasma and Aqueous Samples, Colloid and Interface Science Communications, Vol.46, 2022, 100555.

[32] A. Mohammadinezhad, G. B. Marandi, M. Farsadrooh, H. Javadian, Synthesis of Poly(acrylamide-co-itaconic acid)/MWCNTs Superabsorbent Hydrogel Nanocomposite by Ultrasound-Assisted Technique: Swelling Behaviour and Pb(II) Adsorption Capacity, Ultrasonics Sonochemistry, Vol.49, 2018, pp. 1–12.

[33] A. D. Becke, A New Mixing of Hartree−Fock and Local Density Functional Theories, The Journal of Chemical Physics, Vol.98, No.2, 1993, pp. 1372−1377.

[34] S. A. Halim, A. B. El-Meligy, A. M. El-Nahas, S. H. El-Demerdash, DFT Study, and Natural Bond Orbital (NBO) Population Analysis of 2-(2-Hydroxyphenyl)-1-Azaazulene Tautomers and their Mercapto Analouges, Scientific Reports, Vol.14, No.1, 2024, Article number: 219.

[35] C. Lee, W. Yang, R. G. Parr, Development of the Colle Salvetti Correlation-Energy Formula into a Functional of the Electron Density, Physical Review B, Vol.37, No.2, 1988, 785.

[36] M. Frisch, G. W. Trucks, H. B. Schlegel, G. E. Scuseria, M. A. Robb, J. R. Cheeseman, G. Scalmani, V. Barone, B. Mennucci, G. A. Petersson, Gaussian 09, Gaussian. Inc., Wallingford CT, Vol.121, pp. 150-166, 2009.

[37] G. Mishra, M. Mukhopadhyay, TiO2 Decorated Functionalized Halloysite Nanotubes (TiO2@ HNTs) and Photocatalytic PVC Membranes Synthesis, Characterization and Its Application in Water Treatment, Scientific Reports, Vol.9, No.1, 2019, pp. 1–17.

[38] J. F. Corbett, Pseudo First-Order Kinetics, Journal of Chemical Education, Vol.49, No.10, 1972, 663.

[39] A. K. Greaves, R. J. Letcher, Comparative Body Compartment Composition and In Ovo Transfer of Organophosphate Flame Retardants in North American Great Lakes Herring Gulls, Environmental Science & Technology, Vol.48, No.14, 2014, pp. 7942−7950.

[40] E. Cequier, A. C. Ionas, A. Covaci, R. M. Marce, G. Becher, C.´ Thomsen, Occurrence of a Broad Range of Legacy and Emerging Flame Retardants in Indoor Environments in Norway. Environmental Science & Technology, Vol.48, No.12, 2014, pp. 6827−6835.

[41] J.-W. Kim, T. Isobe, K.-H. Chang, A. Amano, R. H. Maneja, P. B. Zamora, F. P. Siringan, S. Tanabe, Levels and Distribution of Organophosphorus Flame Retardants and Plasticizers in Fishes from Manila Bay, the Philippines, Environmental Pollution, Vol.159, No.12, 2011, pp. 3653-3659.

[42] Q. Wang, J. C.-W. Lam, Y.-C. Man, N. L.-S. Lai, K. Y. Kwok, Y. Y. Guo, P. K.-S. Lam, B. Zhou, Bioconcentration, Metabolism and Neurotoxicity of the Organophorous Flame Retardant 1,3-Dichloro 2-propyl Phosphate (TDCPP) to Zebrafish, Aquatic Toxicology, Vol.158, 2015, pp. 108−115.

[43] N. Van den Eede, W. Maho, C. Erratico, H. Neels, A. Covaci, First Insights in the Metabolism of Phosphate Flame Retardants and Plasticizers Using Human

Liver Fractions. Toxicology Letters, Vol.223, No.1, 2013, pp. 9−15.

[44] M. P. Meyer, L. Gibilaro, I. Massot, P. Pasquet, S. Tailhades, P. Bouvet, Chamelot, Comparative Study on the Chemical Stability of Fe3O4 and NiFe2O4 in Molten Salts, Materials Science and Engineering: B — Advanced Functional Solid-State Materials, Vol.228, 2018, pp. 117–122.

[45] H. Chakhtouna, H. Benzeid, N. Zari, A. Qaiss, R. Bouhfid, R., Functional CoFe2O4-Modified Biochar Derived from Banana Pseudostem as an Efficient Adsorbent for the Removal of Amoxicillin from Water, Separation and Purification Technology, Vol.266, 2021, 118592.

[46] S. Xia, J. Tao, Y. Zhao, Y. Men, C. Chen, Y. Hu, G. Zhu, Y. Chu, B. Yan, G. Chen, Application of Waste Derived Magnetic Acid-Base Bifunctional CoFe/Biochar/CaO as an Efficient Catalyst for Biodiesel Production from Waste Cooking Oil, Chemosphere, Vol.350, 2024, 141104.

[47] H. Peng, Y. Li, J. Wen, X. Zheng, Synthesis of ZnFe2O4/B, N-Codoped Biochar via Microwave-Assisted Pyrolysis for Enhancing Adsorption-Photocatalytic Elimination of Tetracycline Hydrochloride, Industrial Crops and Products, Vol.172, 2021, 114066.

[48] Y. Li, S. Ma, S. Xu, H. Fu, Z. Li, K. Li, K. Sheng, J. Du, X. Lu, X. Li, S. Liu, Novel Magnetic Biochar as an Activator for Peroxymonosulfate to Degrade Bisphenol A: Emphasizing the Synergistic Effect between Graphitized Structure and CoFe2O4, Chemical Engineering Journal, 2020, 387.

[49] Y. Belaiche, K. Minaoui, M. Ouadou, Y. Mouhib, M. Elansary, Elaboration and Experimental Investigation of Zn-Ni-Co Spinel Ferrite Multi-Doped Rare-Earth (Gd, Er, and Sm) Prepared by Coprecipitation Method, Journal of Superconductivity and Novel Magnetism, Vol.35, 2022, pp. 1269–1280.

[50] P. Mishra, A. Behera, D. Kandi, K. Parida, Facile Construction of a Novel NiFe2O4@P-Doped g-C3N4 Nanocomposite with Enhanced Visiblelight Driven Photocatalytic Activity, Chemical Engineering Journal, Vol.497, 2024, 155690.

[51] B. Biswas, M. F. Ahmed, M. L. Rahman, J. Khanam, M. H. R. Bhuiyan, N. Sharmin, Investigation of Structural, Optical, and Magnetic Properties of NiFe2O4 for Efficient Photocatalytic Degradation of Organic Pollutants Through Photo Fenton Reactions, Heliyon, Vol.10, 2024, e37199.

[52] X. Wang, H. Ji, F. Wang, X. Cui, Y. Liu, X. Du, X. Lu, NiFe2O4-Based Magnetic Covalent Organic Framework Nanocomposites for the Efficient Adsorption of Brominated Flame Retardants from Water, Microchim Acta , Vol.188, 2021, 161.

[53] A. Nurmayansih, P. L. Hariani, M. Said, Synthesis NiFe2O4 Nanoparticles by Co-precipitation Method for Degradation of Congo Red Dye, Indonesian Journal of Fundamental and Applied Chemistry, Vol.6, No.3, 2021, pp. 115-121.

[54] A. Ganesh, S. M. Simon, N. John, R. Rajan, S. Thankachan, Development and Characterization of MoO3/NiFe2O4 Nanocomposite Photocatalyst for Organic Pollutants Removal towards Sustainable Water Remediation, Research Square, 2024, pp. 1-20.

[55] E. Derakhshani, A. Naghizadeh, Recent Advancement in NiFe2O4-Based Nanocomposites for the Photocatalytic Degradation of Pollutants in Aqueous Solutions: A Comprehensive Systematic Review, AQUA — Water Infrastructure, Ecosystems and Society, Vol.72, No.8, 2023, pp. 1629-1641.

[56] H. S. Ou, J. Liu, J. S. Ye, L. L. Wang, N. Y. Gao, J. Ke, Degradation of Tris(2-chloroethyl) Phosphate by Ultraviolet-Persulfate: Kinetics, Pathway and Intermediate Impact on Proteome of Escherichia coli. Chemical Engineering Journal, Vol.307, 2017, pp. 386−395.

[57] J. Meyer, K. Bester, Organophosphate Flame Retardants and Plasticisers in Wastewater Treatment Plants, Journal of Environmental Monitoring, Vol.6, No.7, 2004, pp. 599−605.

[58] A. Marklund, B. Andersson, P. Haglund, Organophosphorus Flame Retardants and Plasticizers in Swedish Sewage Treatment Plants. Environmental Science & Technology, Vol.39, No.19, 2005, pp. 7423−7429.

[59] H. Liang, M. A. Rehan, J. Li, S. Du, Y. Zhai, G. Li, Kinetic Simulation of Hydrogen Production Reaction Parameters Based on TiO2 Photocatalyst, Applied Thermal Engineering, Vol.239, 2024, 122134.

[60] M. A. Kumar, C. Ravikumar, H. Nagaswarupa, B. Purshotam, B. Gonfa, H. A.

Murthy, F. K. Sabir, S. Tadesse, Evaluation of Bi-Functional Applications of ZnO Nanoparticles Prepared by Green and Chemical Methods, Journal of Environmental Chemical Engineering, Vol.7, No.6, 2019, 103468.

[61] V. Dileepkumar, P. Surya, C. Pratapkumar, R. Viswanatha, C. Ravikumar, M. A. Kumar, H. Muralidhara, I.M. Al-Akraa, A.M. Mohammad, Z. Chen, NaFeS2 as a New Photocatalytic Material for the Degradation of Industrial Dyes, Journal of Environmental Chemical Engineering, Vol.8, No.4, 2020, 104005.

[62] S. Bhosale, D. Bankar, S. Bhoraskar, V. Mathe, Analysis of Electrokinetic Properties of NiFe2O4 Nanoparticles Synthesized by DC Thermal Plasma Route and Its Use in Adsorption of Humic Substances, Journal of Environmental Chemical Engineering, Vol.4, No.2, 2016, pp. 1584–1593.

[63] R. Zandipak, S. Sobhanardakani, Synthesis of NiFe2O4 Nanoparticles for Removal of Anionic Dyes from Aqueous Solution, Desalination and Water Treatment, Vol.57, No.24, 2016, pp. 11348–11360.

[64] J. Sirajudeen, H. Nagaswarupa, M.A. Kumar, C.R. Kumar, K. Gurushantha, T. S. Shekhar, K. Anantharaju, K.V. Mahesh, S. Sharma, H. Nagabhushana, Photocatalytic and Photoluminescence Studies of ZnO Nanomaterials by Banana Peel Powder, Materials Today: Proceedings, Vol.4, No.11, 2017, pp. 11827–11836.

[65] K. Girish, S. Prashantha, H. Nagabhushana, C. Ravikumar, H. Nagaswarupa, R. Naik, H. Premakumar, B. Umesh, Multi-Functional Zn2TiO4: Sm3+ Nanopowders: Excellent Performance as an Electrochemical Sensor and an UV Photocatalyst, Journal of Science, Vol.3, No.2, (2018, pp. 151–160.

[66] M. A. Kumar, B. Mahendra, H. Nagaswarupa, B. Surendra, C. Ravikumar, K. Shetty, Photocatalytic Studies of MgO Nano Powder; Synthesized by Green Mediated Route, Materials Today: Proceedings, Vol.5, No.10, 2018, pp. 22221–22228.

[67] J. Cristale, D. D. Ramos, R. F. Dantas, A. Machulek Junior, S. Lacorte, C. Sans, S. Esplugas, Can Activated Sludge Treatments and Advanced Oxidation Processes Remove Organophosphorus Flame Retardants?, Environmental Research, Vol.144, 2016, pp. 11−18.

[68] L. Gao, Y. Shi, W. Li, J. Liu, Y. Cai, Occurrence and Distribution of Organophosphate Triesters and Diesters in Sludge from Sewage Treatment Plants of Beijing, China, Science of the Total Environment, Vol.544, 2016, pp. 143−149.

[69] X. Zeng, Z. Liu, L. He, S. Cao, H. Song, Z. Yu, G. Sheng, J. Fu, The Occurrence and Removal of Organophosphate Ester Flame Retardants/Plasticizers in a Municipal Wastewater Treatment Plant in the Pearl River Delta, China, Journal of Environmental Science and Health. Part A Toxic/Hazardous Substances and Environmental Engineering, Vol.50, No.12, 2015, pp. 1291−1297.

[70] E. Martinez-Carballo, C. Gonzalez-Barreiro, A. Sitka, S. Scharf, O. Gans, Determination of Selected Organophosphate Esters in the Aquatic Environment of Austria, Science of the Total Environment, Vol.388, No.1-3, 2007, pp. 290−299.

[71] K. Liang, J. Liu, Understanding the Distribution, Degradation and Fate of Organophosphate Esters in an Advanced Municipal Sewage Treatment Plant Based on Mass Flow and Mass Balance Analysis, Science of the Total Environment, Vol.544, 2016, pp. 262−270.

[72] G. Absalan, M. Asadi, S. Kamran, L. Sheikhian, D.M. Goltz, Removal of Reactive Red-120 and 4-(2-Pyridylazo) Resorcinol from Aqueous Samples by Fe3O4 Magnetic Nanoparticles Using Ionic Liquid as Modifier, Journal of Hazardous Materials, Vol.192, No.2, 2011, pp. 476–484.

[73] C.-Y. Chen, J.-C. Chang, A.-H. Chen, Competitive Biosorption of Azo Dyes from Aqueous Solution on the Templated Crosslinked-Chitosan Nanoparticles, Journal of Hazardous Materials, Vol.185, No.1, 2011, pp. 430–441.

[74] C. Namasivayam, D. Arasi, Removal of Congo Red from Wastewater by Adsorption onto Waste Red Mud, Chemosphere, Vol.34, No.2, 1997, pp. 401–417.

[75] M. Carrier, C. Guillard, M. Besson, C. Bordes, H. Chermette, Photocatalytic Degradation of Diuron: Experimental Analyses and Simulation of HO Radical Attacks by Density Functional Theory Calculations, Journal of Physical Chemistry A, Vol113, No.22, 2009, pp. 6365−6374.

[76] A. Koppaka, J. K. Kirkland, R. A. Periana, D. H. Ess, Experimental Demonstration and Density Functional Theory Mechanistic Analysis of Arene C−H Bond Oxidation and Product Protection by Osmium Tetroxide in a Strongly Basic/Nucleophilic Solvent, Journal of Organic Chemistry, Vol.87, No.21, 2022, pp. 13573−13582.

[77] Q. Liu, J. Liggio, K. Li, P. Lee, S.-M. Li, Understanding the Impact of Relative Humidity and Coexisting Soluble Iron on the OH Initiated Heterogeneous Oxidation of Organophosphate Flame Retardants, Environmental Science & Technology, Vol.53, No.12, 2019, pp. 6794−6803.

[78] A. M. Garbou, M. Liu, S. Zou, C. L. Yestrebsky, Degradation Kinetics of Hexachlorobenzene Over Zero-Valent Magnesium/Graphite in Protic Solvent System and Modeling of Degradation Pathways Using Density Functional Theory, Chemosphere, Vol.222, 2019, pp. 195−204.

[79] M. Antonopoulou, P. Karagianni, I. K. Konstantinou, Kinetic and Mechanistic Study of Photocatalytic Degradation of Flame Retardant Tris (1-chloro-2-propyl) phosphate (TCPP), Applied Catalysis B: Environmental, Vol.192, 2016, pp. 152−160.

Contribution of Individual Authors to the Creation of a Scientific Article (Ghostwriting Policy)

Prof. Dr. Delia Teresa Sponza and Post-Dr. Rukiye Öztekin took an active role in every stage of the preparation of this article.

The authors equally contributed in the present research, at all stages from the formulation of the problem to the final findings and solution.

Sources of Funding for Research Presented in a Scientific Article or Scientific Article Itself

The experimental phases of this research study were conducted at the National Research Council (NRC) of Canada, Research Centers, Ontario, Canada. The authors would like to thank this body for providing financial support.

Conflict of Interest

The authors have no conflicts of interest to declare that are relevant to the content of this article.

APPENDIX

Table 1. The classification of toxicity values

Toxicity Level	**Toxicity Ranges**
Very toxic	$LC_{50}/EC_{50}/ChV \leq 1$
Toxic	$1 < LC_{50}/EC_{50}/ChV \leq 10$
Harmful	$10 < LC_{50}/EC_{50}/ChV \leq 100$
Not harmful	$LC_{50}/EC_{50}/ChV > 100$

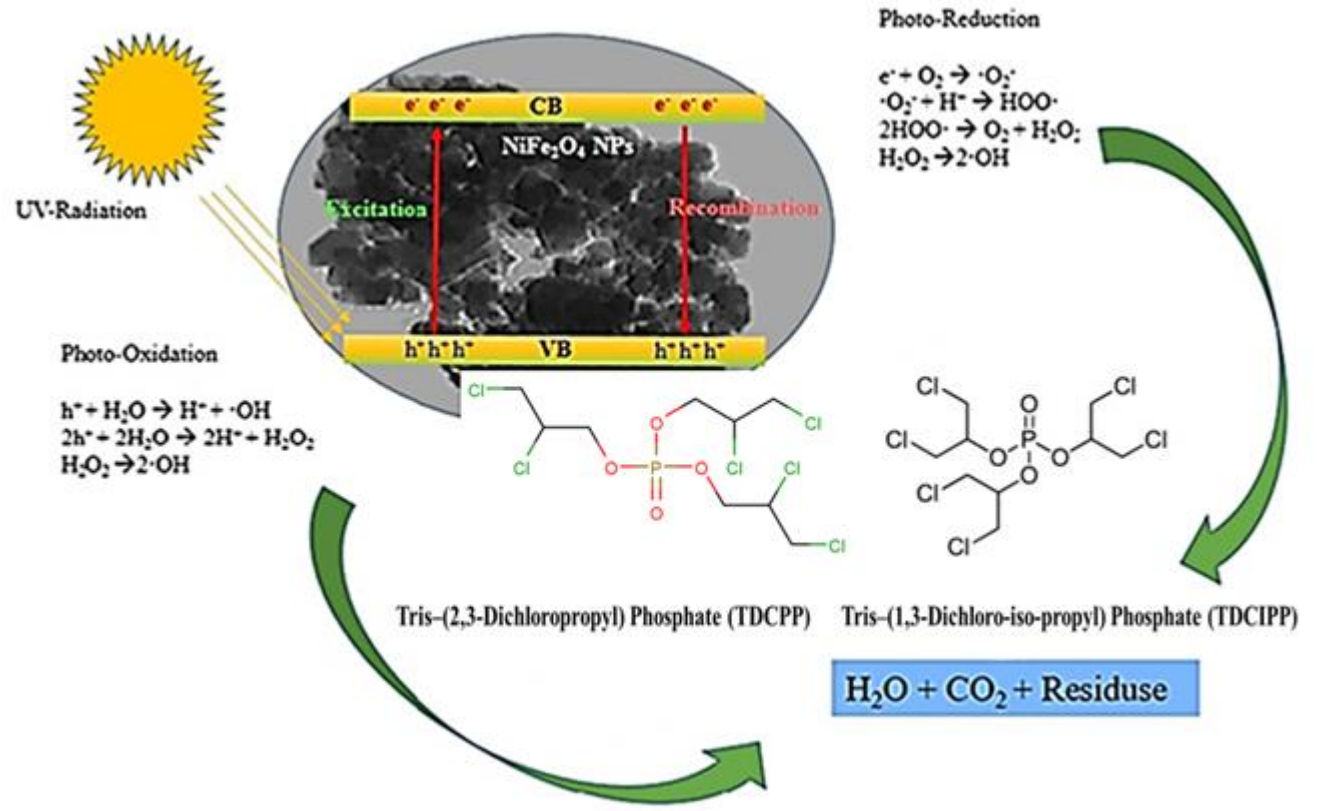

Fig. 1: The mechanism of the photodegradation of TDCPP and TDCIPP on the NiFe2O4–MCOF NC under UV-light irradiation

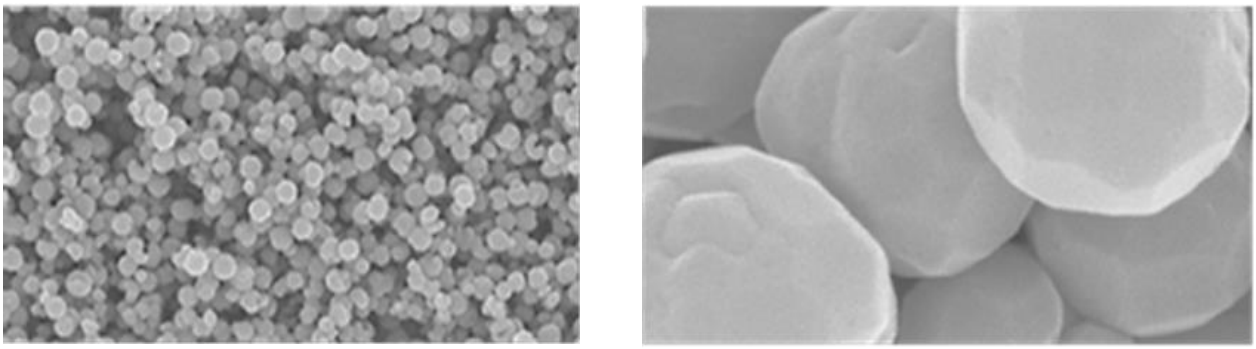

(a) **(b)**

Fig. 2: SEM results of NiFe2O4 (a) and NiFe2O4-MCOF NC (b)

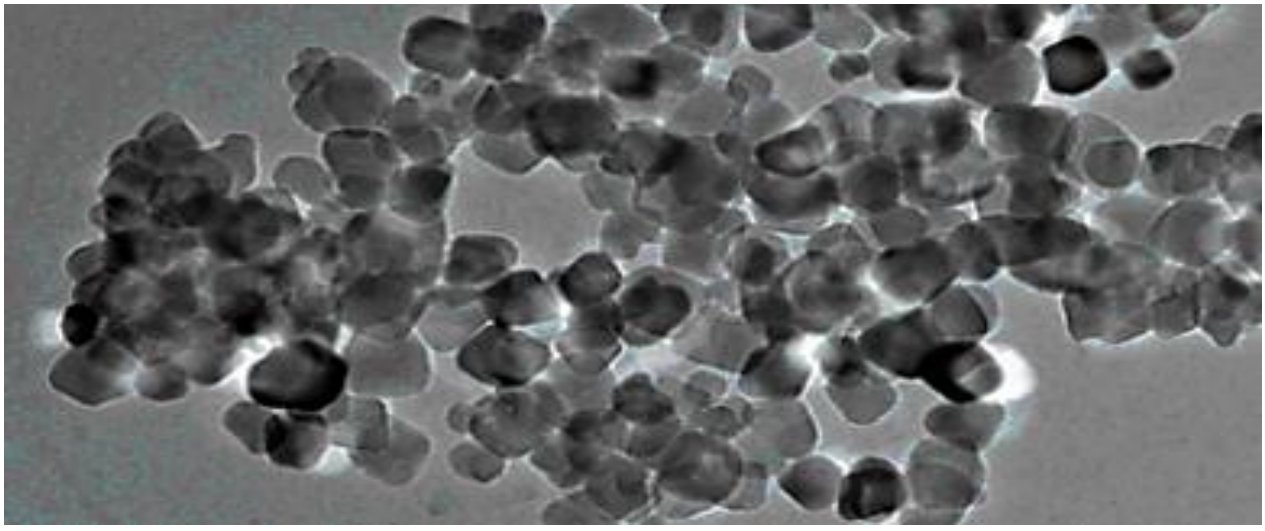

(a)

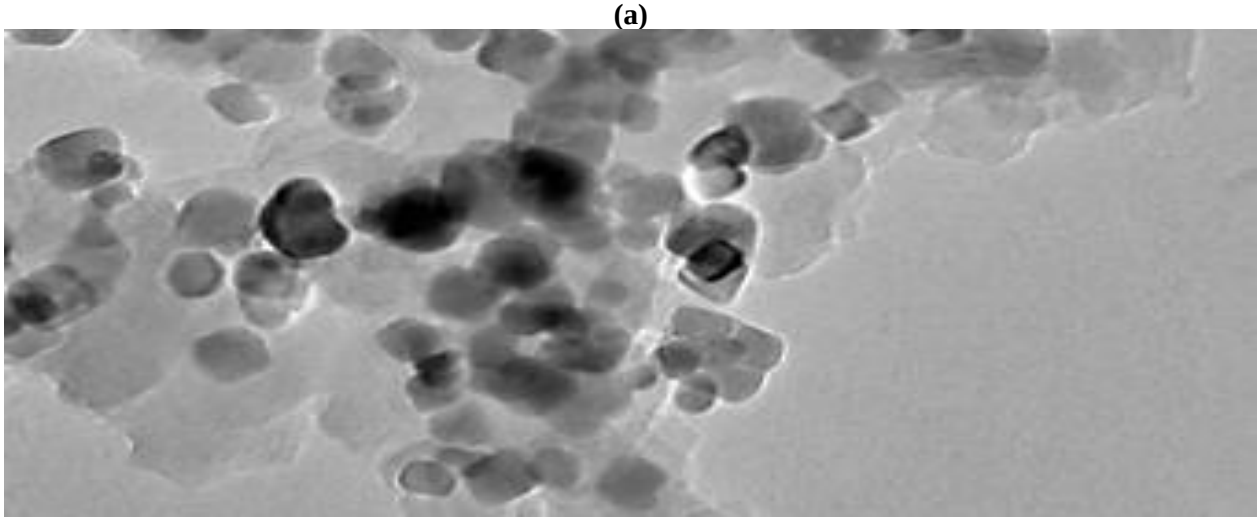

(b)

Fig. 3: TEM data of NiFe2O4 (a) and NiFe2O4–MCOF NC (b)

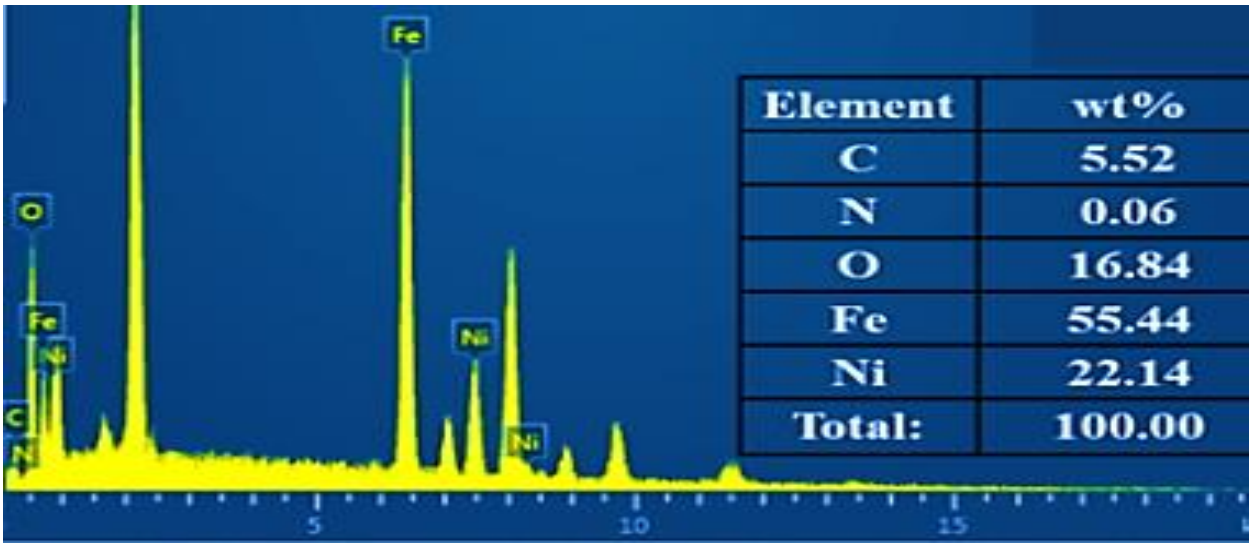

(a)

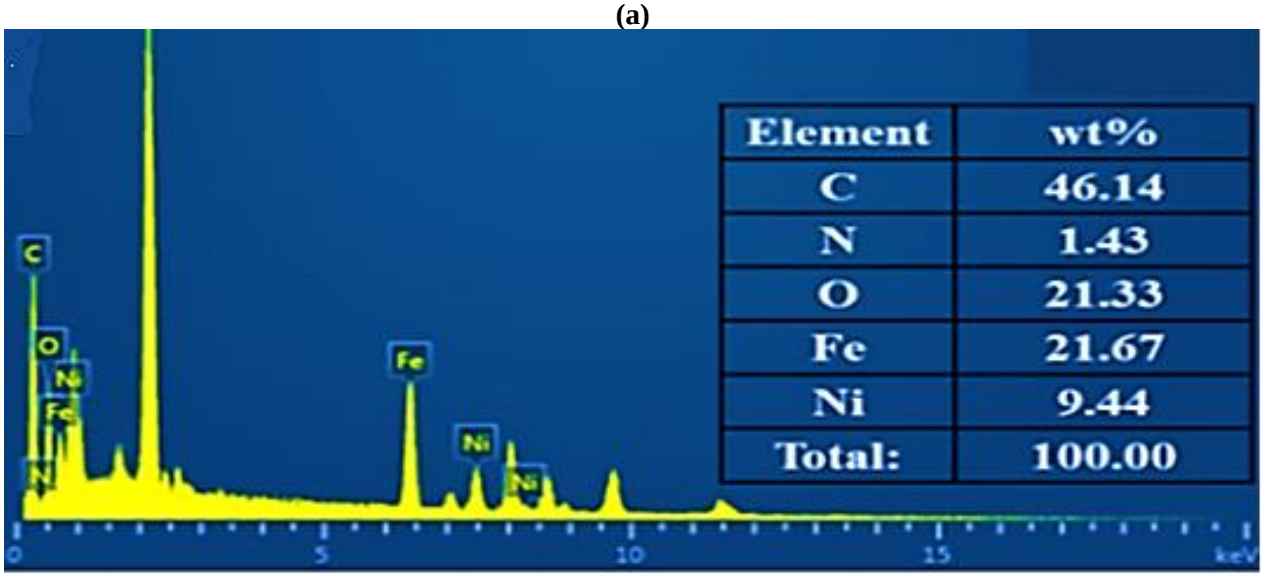

(b)

Fig. 4: EDS data of NiFe2O4 (a) and NiFe2O4–MCOF NC (b)

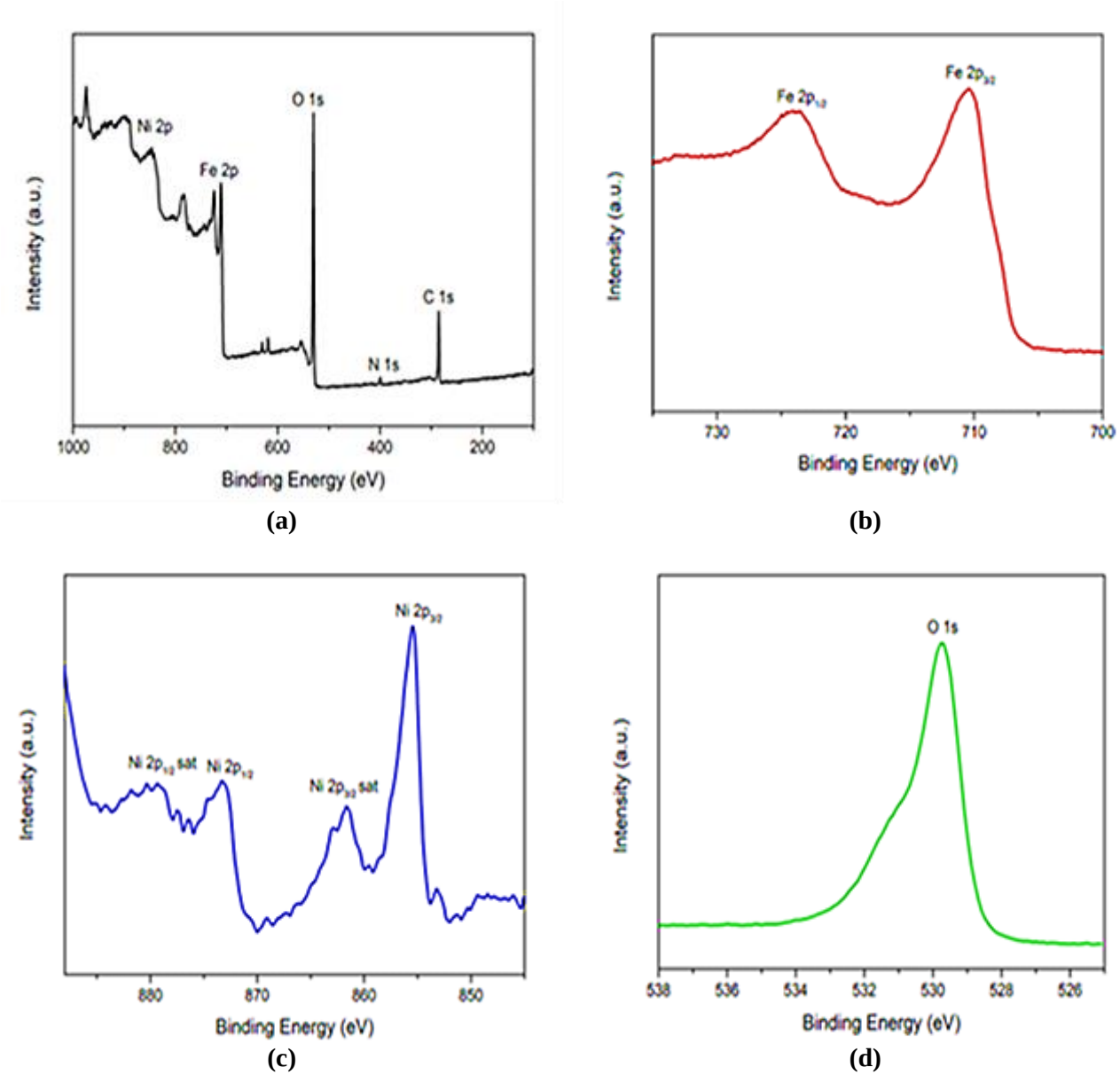

Fig. 5: XPS results existence of Fe, Ni, O, C and N elements (a), XPS spectrum of Fe 2p orbital (b), the narrow scan XPS spectrum of Ni 2p orbital (c), Ni 2p1/2 and Ni 2p3/2 of trivalent Ni signals (d)

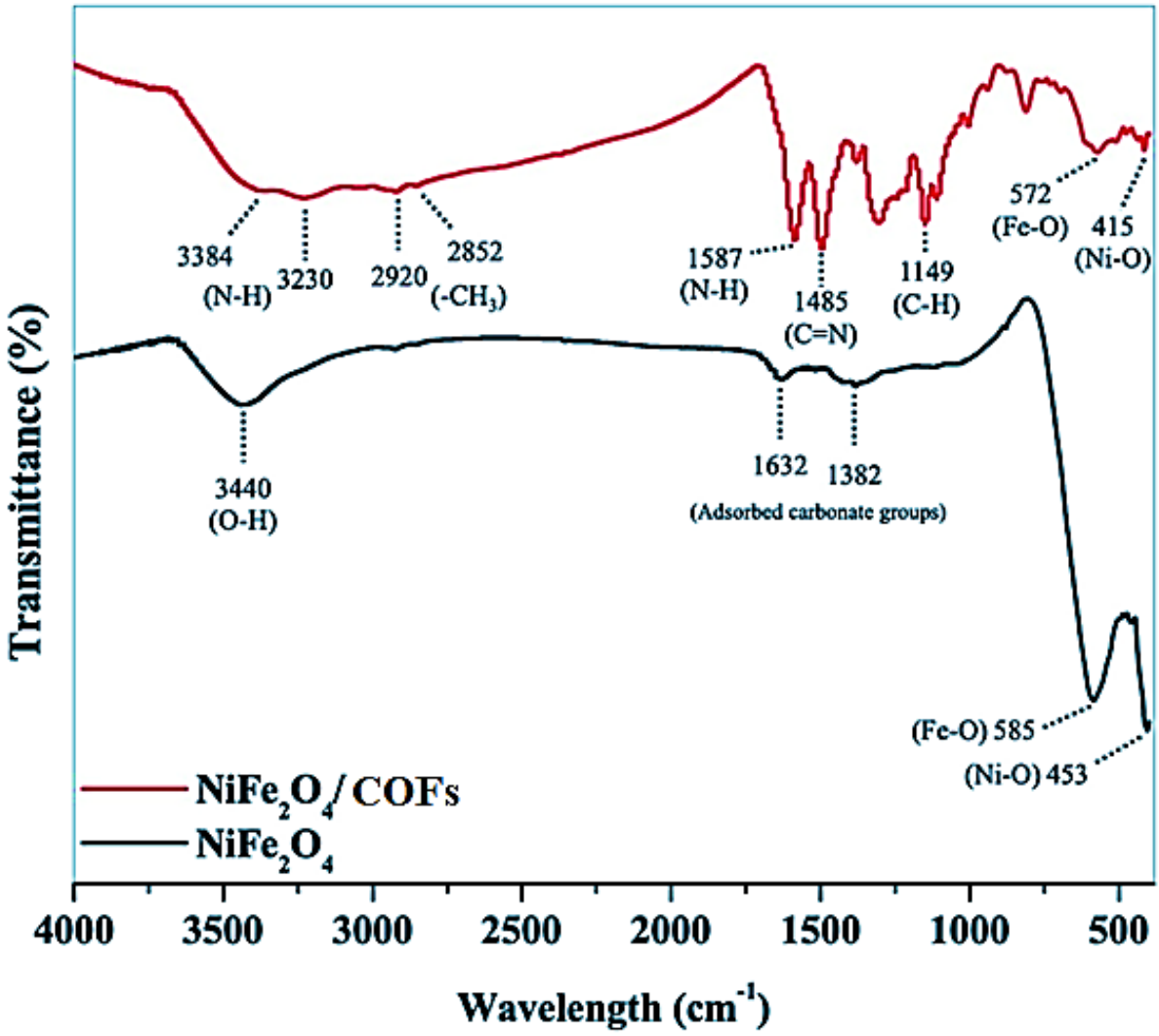

Fig. 6: FTIR spectra of NiFe2O4 and NiFe2O4–MCOF NC

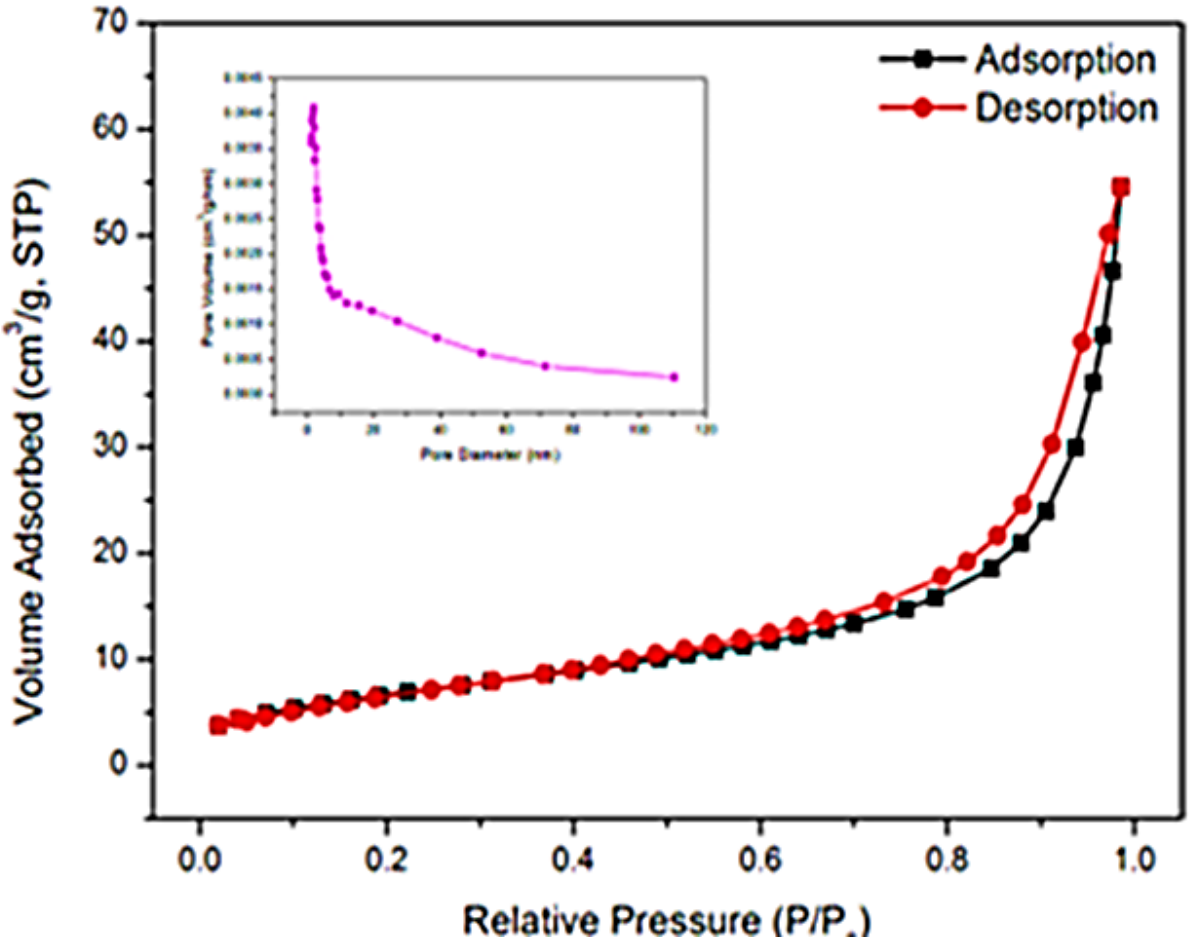

Fig. 7: Photocatalytic adsorption and desorption isotherms of NiFe2O4–MCOF NC

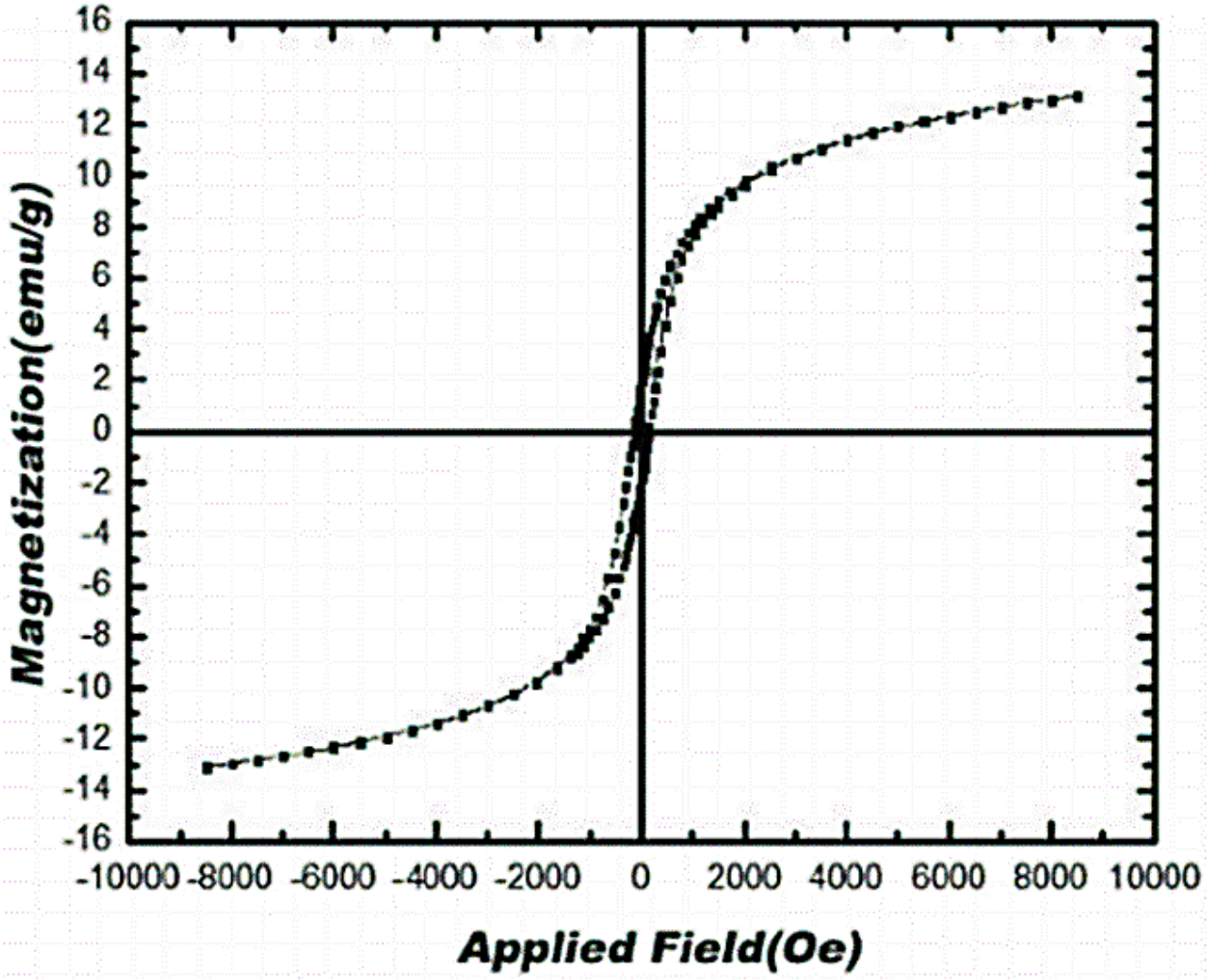

Fig. 8: VSM curves of NiFe2O4–MCOF NC

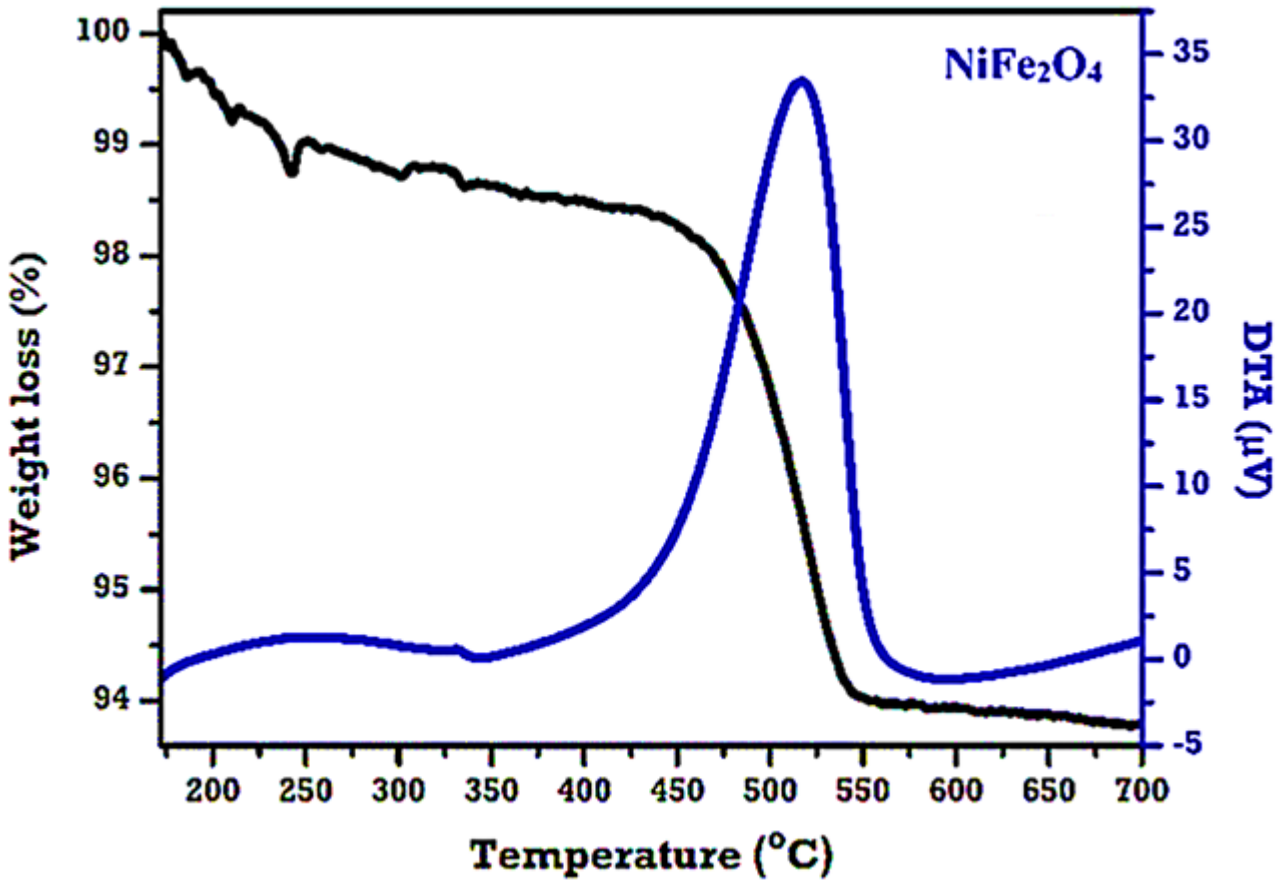

Fig. 9: TGA analysis (black line) of NiFe2O4 (a) and DTA analysis (blue line) of NiFe2O4 (b)

Table 2. The obtained kinetic parameters for adsorption during photodegradation of TDCPP and TDCIPP (1500 mg/l)

Data	**Pseudo-first-order**			**Pseudo-second-order**			**Intra particle diffusion**		
	q_e (mg/g)	k_1 (min^{-1})	R^2	q_e (mg/g)	k_2 (min^{-1})	R^2	k_{diff} (min^{-1})	C (mg/l)	R^2
TDCPP	9.3	0.014	0.9752	22.677	0.115	0.9978	0.0018	10.031	0.8070
TDCIPP	9.1	0.012	0.9840	22.701	0.113	0.9919	0.0019	10.027	0.8145

Table 3. Photodegradation kinetics of TDCPP and TDCIPP

TDCPP and TDCIPP Concentrations (mg/l)	**$NiFe_2O_4$–MCOF NC Concentration (mg/l)**	**TDCPP Photodegradation Rate (min^{-1})**	**TDCIPP Photodegradation Rate (min^{-1})**
500	0.1	0.02	0.019
1000	0.5	0.05	0.04
1500	1.0	0.09	0.09
2000	1.5	0.03	0.02
3000	2.0	0.02	0.01

Table 4. Effects of TDCPP and TDCIPP concentrations on photodegradation yields of TDCPP and TDCIPP after 5 min

TDCPP and TDCIPP Concentrations (mg/l)	**TDCPP Photodegradation Yields (%)**	**TDCIPP Photodegradation Yields (%)**
500	99	99
1000	99	99
1500	99	98
2000	78	73
3000	70	68

Table 5. Effect of pH on photodegradation the TDCPP and TDCIPP

pH	**TDCPP Photodegradation Yields (%)**	**TDCIPP Photodegradation Yields (%)**
4.0	45	40
5.0	80	76
6.0	99	98
7.0	65	63
8.0	53	50

Table 6. Effect of temperature on photodegradation of TDCPP and TDCIPP

Temperature (°C)	**TDCPP Photodegradation Yields (%)**	**TDCIPP Photodegradation Yields (%)**
20	45	40
30	80	76
40	99	98
55	65	63
70	53	50

Table 7. Effect of contacting time on photodegradation of TDCPP and TDCIPP

Contacting time (min)	**TDCPP Photodegradation Yields (%)**	**TDCIPP Photodegradation Yields (%)**
1	45	40
2	60	70
5	99	98
30	98	97
60	98	97

Table 8. Effect of NiFe2O4–MCOF NC concentration

$NiFe_2O_4$–MCOF NC Concentration (mg/l)	**TDCPP Photodegradation Yields (%)**	**TDCIPP Photodegradation Yields (%)**
0.1	45	40
0.3	60	70
0.5	90	90
1.0	99	97
2.0	80	79

Table 9. Reusability of NiFe2O4–MCOF NCs

Cycles	**TDCPP Photodegradation Yields (%)**	**TDCIPP Photodegradation Yields (%)**
1	99	97
2	99	97
3	99	97
4	99	97
5	99	97
6	99	97
7	99	97
8	99	97
9	99	97
10	99	97
11	99	97
12	99	97
13	99	97
14	99	97
15	99	97
16	97	95
17	97	95
18	97	94
19	96	94
20	96	94

Table 10. The intermediates of TDCPP and TDCIPP

TDCPP Intermediates	**TDCIPP Intermediates**
TP313 ($C_6H_{10}Cl_3O_6P$)	Bis(1,3-dichloro-2-propyl) phosphate (BDCPP)
TP207 ($C_3H_7Cl_2O_4P$)	Tris(2,3-dibromopropyl) phosphate (TDBPP)
1,3-dichloro-2-propanol (1,3-DCP)	Tris(2-chloroethyl) phosphate (TCEP)
3-monochloropropane-1,2-diol (3-MCPD) or 3-monochloro-1,2-propanediol (3-MCPD)	1,3-dichloro-2-propyl-phosphate (MDCPP)
Glutathione-S-alkyl transferase	Tris(1-chloro-2-propyl) phosphate (TCPP)
Epichlorohydrin	1,3-dichloroacetone
Glycidol	Glutathione
β-chlorolactaldehyde	Ninhydrin
Glycerol	Mercapturic acid

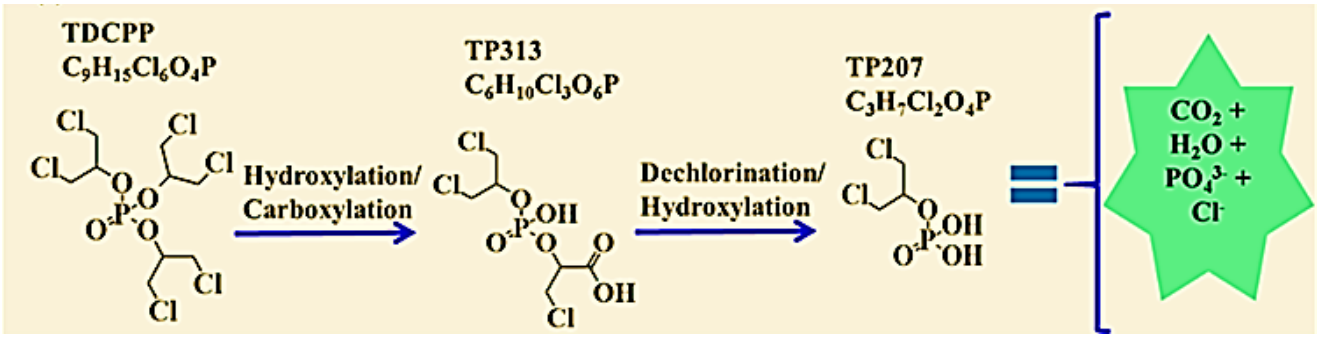

Fig. 10: Proposed degradation intermediate pathways of 1000 mg/l TDCPP using 1.0 mg/l NiFe2O4–MCOF NC as a catalyst under UV light and the DFT prediction of TDCPP molecular structure

Table 11. Chloride ion (Cl-) concentrations in 500 mg/l TDCPP with 1.0 mg/l NiFe2O4–MCOF NCs

	Ion releasing concentration (µM)	
Experimental samples	Cl^-	PO_4^{3-}
TDCPP before UV-vis irradiation	0.26	0.06
TDCPP after 60 min UV-vis irradiation time	0.27	0.08
TDCPP+P25 after 60 min UV-vis irradiation time	2.34	0.36
TDCPP before UV-vis irradiation	0.28	0.07
TDCPP after 60 min UV-vis irradiation time	0.29	0.09
TDCPP+P25 after 60 min UV-vis irradiation time	2.52	0.42

Table 12. Comparison of acute and chronic toxicities of TDCPP and TDCIP and their degradation intermediates by using the ECOSAR predictive model

Chemicals	**Intermediates**	**Acute Toxicity (mg/l)**			**Chronic Toxicity (mg/l)**		
		Daphnid (LC_{50})	**Fish (LC_{50})**	**Green Algae (EC_{50})**	**Daphnid (ChV) [a]**	**Fish (ChV) [a]**	**Green Algae (ChV) [a]**
TDCPP		10.8	5.29	3.96	2.03	0.44	1.47
	TP313	19785	39254	8912	1384	3326	1784
	TP207	1267	2541	571	88.5	210	113
TDCIPP		11.6	5.34	4.02	2.75	0.52	1.90
	BDCPP	20962	41312	9226	1412	3540	1846
	TDBPP	1354	2879	612	97.3	275	126

[a] : The toxicity values are classified into four grades: very toxic, $LC_{50}/EC_{50}/ChV \leq 1$; toxic, $1 < LC_{50}/EC_{50}/ChV \leq 10$; harmful, $10 < LC_{50}/EC_{50}/ChV \leq 100$, not harmful, $LC_{50}/EC_{50}/ChV > 100$, respectively.